EUROPEAN ORGANIZATION FOR NUCLEAR RESEARCH

CERN-EP-2001-023
8 March 2001

Precision Neutral Current Asymmetry Parameter Measurements from the Tau Polarization at LEP

The OPAL Collaboration

Abstract

Measurements of the τ lepton polarization and forward-backward polarization asymmetry near the Z^0 resonance using the OPAL detector are described. The measurements are based on analyses of $\tau \to e\nu_e\nu_\tau$, $\tau \to \mu\nu_\mu\nu_\tau$, $\tau \to \pi\nu_\tau$, $\tau \to \rho\nu_\tau$ and $\tau \to a_1\nu_\tau$ decays from a sample of $144,810$ $e^+e^- \to \tau^+\tau^-$ candidates corresponding to an integrated luminosity of 151 pb^{-1}. Assuming that the τ lepton decays according to V$-$A theory, we measure the average τ polarization near $\sqrt{s} = M_Z$ to be $\langle P_\tau \rangle = (-14.10 \pm 0.73 \pm 0.55)\%$ and the τ polarization forward-backward asymmetry to be $A_{pol}^{FB} = (-10.55 \pm 0.76 \pm 0.25)\%$, where the first error is statistical and the second systematic. Taking into account the small effects of the photon propagator, photon-Z^0 interference and photonic radiative corrections, these results can be expressed in terms of the lepton neutral current asymmetry parameters:

$$\begin{aligned} \mathcal{A}_\tau &= 0.1456 \pm 0.0076 \pm 0.0057, \\ \mathcal{A}_e &= 0.1454 \pm 0.0108 \pm 0.0036. \end{aligned}$$

These measurements are consistent with the hypothesis of lepton universality and combine to give $\mathcal{A}_\ell = 0.1455 \pm 0.0073$. Within the context of the Standard Model this combined result corresponds to $\sin^2\theta_{eff}^{lept} = 0.23172 \pm 0.00092$. Combing these results with those from the other OPAL neutral current measurements yields a value of $\sin^2\theta_{eff}^{lept} = 0.23211 \pm 0.00068$.

(submitted to the European Physical Journal C)

The OPAL Collaboration

G. Abbiendi[2], C. Ainsley[5], P.F. Åkesson[3], G. Alexander[22], J. Allison[16], G. Anagnostou[1], K.J. Anderson[9], S. Arcelli[17], S. Asai[23], D. Axen[27], G. Azuelos[18,a], I. Bailey[26], A.H. Ball[8], E. Barberio[8], R.J. Barlow[16], R.J. Batley[5], T. Behnke[25], K.W. Bell[20], G. Bella[22], A. Bellerive[9], G. Benelli[2], S. Bethke[32], O. Biebel[32], I.J. Bloodworth[1], O. Boeriu[10], P. Bock[11], J. Böhme[25], D. Bonacorsi[2], M. Boutemeur[31], S. Braibant[8], L. Brigliadori[2], R.M. Brown[20], H.J. Burckhart[8], J. Cammin[3], P. Capiluppi[2], R.K. Carnegie[6], B. Caron[28], A.A. Carter[13], J.R. Carter[5], C.Y. Chang[17], D.G. Charlton[1,b], P.E.L. Clarke[15], E. Clay[15], I. Cohen[22], J. Couchman[15], A. Csilling[15,i], M. Cuffiani[2], S. Dado[21], G.M. Dallavalle[2], S. Dallison[16], A. De Roeck[8], E.A. De Wolf[8], P. Dervan[15], K. Desch[25], B. Dienes[30,f], M.S. Dixit[7], M. Donkers[6], J. Dubbert[31], E. Duchovni[24], G. Duckeck[31], I.P. Duerdoth[16], P.G. Estabrooks[6], E. Etzion[22], F. Fabbri[2], M. Fanti[2], L. Feld[10], P. Ferrari[12], F. Fiedler[8], I. Fleck[10], M. Ford[5], A. Frey[8], A. Fürtjes[8], D.I. Futyan[16], P. Gagnon[12], J.W. Gary[4], G. Gaycken[25], C. Geich-Gimbel[3], G. Giacomelli[2], P. Giacomelli[8], D. Glenzinski[9], J. Goldberg[21], C. Grandi[2], K. Graham[26], E. Gross[24], J. Grunhaus[22], M. Gruwé[08], P.O. Günther[3], A. Gupta[9], C. Hajdu[29], G.G. Hanson[12], K. Harder[25], A. Harel[21], M. Harin-Dirac[4], M. Hauschild[8], C.M. Hawkes[1], R. Hawkings[8], R.J. Hemingway[6], C. Hensel[25], G. Herten[10], R.D. Heuer[25], J.C. Hill[5], K. Hoffman[8], R.J. Homer[1], A.K. Honma[8], D. Horváth[29,c], K.R. Hossain[28], R. Howard[27], P. Hüntemeyer[25], P. Igo-Kemenes[11], K. Ishii[23], A. Jawahery[17], H. Jeremie[18], C.R. Jones[5], P. Jovanovic[1], T.R. Junk[6], N. Kanaya[23], J. Kanzaki[23], G. Karapetian[18], D. Karlen[6], V. Kartvelishvili[16], K. Kawagoe[23], T. Kawamoto[23], R.K. Keeler[26], R.G. Kellogg[17], B.W. Kennedy[20], D.H. Kim[19], K. Klein[11], A. Klier[24], S. Kluth[32], T. Kobayashi[23], M. Kobel[3], T.P. Kokott[3], S. Komamiya[23], R.V. Kowalewski[26], T. Kämer[25], T. Kress[4], P. Krieger[6], J. von Krogh[11], D. Krop[12], T. Kuhl[3], M. Kupper[24], P. Kyberd[13], G.D. Lafferty[16], H. Landsman[21], D. Lanske[14], I. Lawson[26], J.G. Layter[4], A. Leins[31], D. Lellouch[24], J. Letts[12], L. Levinson[24], R. Liebisch[11], J. Lillich[10], C. Littlewood[5], A.W. Lloyd[1], S.L. Lloyd[13], F.K. Loebinger[16], G.D. Long[26], M.J. Losty[7], J. Lu[27], J. Ludwig[10], A. Macchiolo[18], A. Macpherson[28,l], W. Mader[3], S. Marcellini[2], T.E. Marchant[16], A.J. Martin[13], J.P. Martin[18], G. Martinez[17], T. Mashimo[23], P. Mättig[24], W.J. McDonald[28], J. McKenna[27], T.J. McMahon[1], R.A. McPherson[26], F. Meijers[8], P. Mendez-Lorenzo[31], W. Menges[25], F.S. Merritt[9], H. Mes[7], A. Michelini[2], S. Mihara[23], G. Mikenberg[24], D.J. Miller[15], W. Mohr[10], A. Montanari[2], T. Mori[23], K. Nagai[13], I. Nakamura[23], H.A. Neal[33], R. Nisius[8], S.W. O'Neale[1], F.G. Oakham[7], F. Odorici[2], A. Oh[8], A. Okpara[11], M.J. Oreglia[9], S. Orito[23], C. Pahl[32], G. Pásztor[8,i], J.R. Pater[16], G.N. Patrick[20], J.E. Pilcher[9], J. Pinfold[28], D.E. Plane[8], B. Poli[2], J. Polok[8], O. Pooth[8], A. Quadt[8], K. Rabbertz[8], C. Rembser[8], P. Renkel[24], H. Rick[4], N. Rodning[28], J.M. Roney[26], S. Rosati[3], K. Roscoe[16], A.M. Rossi[2], Y. Rozen[21], K. Runge[10], O. Runolfsson[8], D.R. Rust[12], K. Sachs[6], T. Saeki[23], O. Sahr[31], E.K.G. Sarkisyan[8,m], C. Sbarra[26], A.D. Schaile[31], O. Schaile[31], P. Scharff-Hansen[8], M. Schröder[8], M. Schumacher[25], C. Schwick[8], W.G. Scott[20], R. Seuster[14,g], T.G. Shears[8,j], B.C. Shen[4], C.H. Shepherd-Themistocleous[5], P. Sherwood[15], G.P. Siroli[2], A. Skuja[17], A.M. Smith[8], G.A. Snow[17], R. Sobie[26], S. Söldner-Rembold[10,e], S. Spagnolo[20], F. Spano[9], M. Sproston[20], A. Stahl[3], K. Stephens[16], D. Strom[19], R. Ströhmer[31], L. Stumpf[26], B. Surrow[8], S.D. Talbot[1], S. Tarem[21], M. Tasevsky[8], R.J. Taylor[15], R. Teuscher[9], J. Thomas[15], M.A. Thomson[5], E. Torrence[9], S. Towers[6], D. Toya[23], T. Trefzger[31], I. Trigger[8], Z. Trócsányi[30,f], E. Tsur[22], M.F. Turner-Watson[1], I. Ueda[23], B. Vachon[26], C.F. Vollmer[31], P. Vannerem[10], M. Verzocchi[8], H. Voss[8], J. Vossebeld[8], D. Waller[6], C.P. Ward[5], D.R. Ward[5], P.M. Watkins[1], A.T. Watson[1], N.K. Watson[1], P.S. Wells[8], T. Wengler[8], N. Wermes[3], D. Wetterling[11] J.S. White[6], G.W. Wilson[16], J.A. Wilson[1], T.R. Wyatt[16], S. Yamashita[23], V. Zacek[18], D. Zer-Zion[8,k]

[1]School of Physics and Astronomy, University of Birmingham, Birmingham B15 2TT, UK
[2]Dipartimento di Fisica dell' Università di Bologna and INFN, I-40126 Bologna, Italy

[3]Physikalisches Institut, Universität Bonn, D-53115 Bonn, Germany
[4]Department of Physics, University of California, Riverside CA 92521, USA
[5]Cavendish Laboratory, Cambridge CB3 0HE, UK
[6]Ottawa-Carleton Institute for Physics, Department of Physics, Carleton University, Ottawa, Ontario K1S 5B6, Canada
[7]Centre for Research in Particle Physics, Carleton University, Ottawa, Ontario K1S 5B6, Canada
[8]CERN, European Organisation for Nuclear Research, CH-1211 Geneva 23, Switzerland
[9]Enrico Fermi Institute and Department of Physics, University of Chicago, Chicago IL 60637, USA
[10]Fakultät für Physik, Albert Ludwigs Universität, D-79104 Freiburg, Germany
[11]Physikalisches Institut, Universität Heidelberg, D-69120 Heidelberg, Germany
[12]Indiana University, Department of Physics, Swain Hall West 117, Bloomington IN 47405, USA
[13]Queen Mary and Westfield College, University of London, London E1 4NS, UK
[14]Technische Hochschule Aachen, III Physikalisches Institut, Sommerfeldstrasse 26-28, D-52056 Aachen, Germany
[15]University College London, London WC1E 6BT, UK
[16]Department of Physics, Schuster Laboratory, The University, Manchester M13 9PL, UK
[17]Department of Physics, University of Maryland, College Park, MD 20742, USA
[18]Laboratoire de Physique Nucléaire, Université de Montréal, Montréal, Quebec H3C 3J7, Canada
[19]University of Oregon, Department of Physics, Eugene OR 97403, USA
[20]CLRC Rutherford Appleton Laboratory, Chilton, Didcot, Oxfordshire OX11 0QX, UK
[21]Department of Physics, Technion-Israel Institute of Technology, Haifa 32000, Israel
[22]Department of Physics and Astronomy, Tel Aviv University, Tel Aviv 69978, Israel
[23]International Centre for Elementary Particle Physics and Department of Physics, University of Tokyo, Tokyo 113-0033, and Kobe University, Kobe 657-8501, Japan
[24]Particle Physics Department, Weizmann Institute of Science, Rehovot 76100, Israel
[25]Universität Hamburg/DESY, II Institut für Experimental Physik, Notkestrasse 85, D-22607 Hamburg, Germany
[26]University of Victoria, Department of Physics, P O Box 3055, Victoria BC V8W 3P6, Canada
[27]University of British Columbia, Department of Physics, Vancouver BC V6T 1Z1, Canada
[28]University of Alberta, Department of Physics, Edmonton AB T6G 2J1, Canada
[29]Research Institute for Particle and Nuclear Physics, H-1525 Budapest, P O Box 49, Hungary
[30]Institute of Nuclear Research, H-4001 Debrecen, P O Box 51, Hungary
[31]Ludwigs-Maximilians-Universität München, Sektion Physik, Am Coulombwall 1, D-85748 Garching, Germany
[32]Max-Planck-Institute für Physik, Föhring Ring 6, 80805 München, Germany
[33]Yale University,Department of Physics,New Haven, CT 06520, USA

[a] and at TRIUMF, Vancouver, Canada V6T 2A3
[b] and Royal Society University Research Fellow
[c] and Institute of Nuclear Research, Debrecen, Hungary
[e] and Heisenberg Fellow
[f] and Department of Experimental Physics, Lajos Kossuth University, Debrecen, Hungary
[g] and MPI München
[i] and Research Institute for Particle and Nuclear Physics, Budapest, Hungary
[j] now at University of Liverpool, Dept of Physics, Liverpool L69 3BX, UK
[k] and University of California, Riverside, High Energy Physics Group, CA 92521, USA
[l] and CERN, EP Div, 1211 Geneva 23
[m] and Tel Aviv University, School of Physics and Astronomy, Tel Aviv 69978, Israel.

1 Introduction

Parity violation in the weak neutral current results in a polarization of final-state fermion−anti-fermion pairs produced in Z^0 decay with the τ lepton being the only fundamental fermion whose polarization is experimentally accessible using the detectors at the LEP e^+e^- collider. Consequently, measurements of the τ polarization provide a means for determining neutral current asymmetry parameters which depend on the neutral current vector and axial vector coupling constants. In the Standard Model the effective electroweak mixing angle is determined from these couplings, therefore the polarization measurements yield a value of $\sin^2\theta_{\rm eff}^{\rm lept}$.

The τ polarization, P_τ, is defined as $P_\tau \equiv (\sigma_+ - \sigma_-)/(\sigma_+ + \sigma_-)$, where $\sigma_{+(-)}$ represents the cross-section for producing positive(negative) helicity τ^- leptons[1]. Assuming unpolarized e^+e^- beams, the spin-1 nature of the intermediate state implies that the lowest order differential cross-sections for σ_+ and σ_- can be expressed as:

$$\begin{aligned}
\frac{1}{\sigma_{total}}\frac{d\sigma_+}{d\cos\theta_{\tau^-}} &= \tfrac{3}{16}[(1+\langle P_\tau\rangle\ )(1+\cos^2\theta_{\tau^-}) + \tfrac{8}{3}(\mathrm{A_{FB}}\ + \mathrm{A_{pol}^{FB}}\ )\cos\theta_{\tau^-}] \\
\frac{1}{\sigma_{total}}\frac{d\sigma_-}{d\cos\theta_{\tau^-}} &= \tfrac{3}{16}[(1-\langle P_\tau\rangle\ )(1+\cos^2\theta_{\tau^-}) + \tfrac{8}{3}(\mathrm{A_{FB}}\ - \mathrm{A_{pol}^{FB}}\ )\cos\theta_{\tau^-}] \qquad (1)
\end{aligned}$$

where θ_{τ^-} is the angle between the e^- beam and the final-state τ^-; $\sigma_{total} = [\sigma_+ + \sigma_-]_{-1<\cos\theta_{\tau^-}<1}$; $\langle P_\tau\rangle$ is the average τ polarization,

$$\langle P_\tau\rangle \equiv \frac{[\sigma_+]_{-1<\cos\theta_{\tau^-}<1} - [\sigma_-]_{-1<\cos\theta_{\tau^-}<1}}{\sigma_{total}};$$

$\mathrm{A_{FB}}$ is the forward-backward asymmetry of the τ-pairs,

$$\mathrm{A_{FB}} \equiv \frac{[\sigma]_{\cos\theta_{\tau^-}>0} - [\sigma]_{\cos\theta_{\tau^-}<0}}{\sigma_{total}};$$

and $\mathrm{A_{pol}^{FB}}$ is the forward-backward τ polarization asymmetry,

$$\mathrm{A_{pol}^{FB}} \equiv \frac{[\sigma_+ - \sigma_-]_{\cos\theta_{\tau^-}>0} - [\sigma_+ - \sigma_-]_{\cos\theta_{\tau^-}<0}}{\sigma_{total}}.$$

Equation 1 implies a simple dependence of P_τ on $\cos\theta_{\tau^-}$:

$$P_\tau(\cos\theta_{\tau^-}) = \frac{\langle P_\tau\rangle\ (1+\cos^2\theta_{\tau^-}) + \frac{8}{3}\mathrm{A_{pol}^{FB}}\ \cos\theta_{\tau^-}}{(1+\cos^2\theta_{\tau^-}) + \frac{8}{3}\mathrm{A_{FB}}\ \cos\theta_{\tau^-}} \qquad (2)$$

where the three parameters, $\langle P_\tau\rangle$, $\mathrm{A_{pol}^{FB}}$ and $\mathrm{A_{FB}}$ are extracted from data. These parameters include contributions from Z^0 exchange, photon exchange and photon-Z^0 interference, as well as from photonic radiative corrections. At LEP 1, where $\sqrt{s}$ is near M_Z, the pure Z^0 exchange term dominates the polarization. Nonetheless, the small contributions arising from the other components must still be taken into account in the interpretation of these parameters in the context of the neutral current couplings. The effects of the $\sqrt{s}$ dependence of the relative sizes of these contributions, which are non-negligible near the Z^0 pole, must also be considered for a precise neutral current interpretation.

[1]By convention, $P_\tau = P_{\tau^-}$ and since, to a very good approximation, the τ^- and τ^+ in a given event have opposite helicities at LEP: $P_{\tau^-} = -P_{\tau^+}$.

When only the pure Z^0 exchange is considered, the interpretation of the measured values of $\langle P_\tau \rangle$ and A_{pol}^{FB} in terms of the neutral current asymmetry parameters $\mathcal{A}_\tau$ and $\mathcal{A}_e$ is remarkably simple:

$$\langle P_\tau \rangle = -\mathcal{A}_\tau \qquad \text{and} \qquad A_{pol}^{FB} = -\frac{3}{4}\mathcal{A}_e \tag{3}$$

where the asymmetry parameters are defined[1] as:

$$\mathcal{A}_\ell \equiv \frac{2 g_{V\ell}/g_{A\ell}}{1 + (g_{V\ell}/g_{A\ell})^2} \tag{4}$$

and the symbols $g_{V\ell}$ and $g_{A\ell}$ represent the effective neutral current vector and axial vector couplings for lepton ℓ as defined in reference [1].

The inequality of the Z^0 coupling to left-handed and right-handed initial-state electrons results in a polarization of the Z^0 which manifests itself as A_{pol}^{FB}, whereas $\langle P_\tau \rangle$ expresses the inequality of the Z^0 coupling to the two chiral states of the final state τ leptons. Therefore, once the small effects of photon exchange, photon-Z^0 interference and photonic radiative corrections are taken into account, the measurement of $\langle P_\tau \rangle$ is directly related to the ratio of the vector to axial vector coupling constants for τ leptons and that of A_{pol}^{FB} to the ratio for electrons [2]. Consequently, these measurements test the hypothesis of lepton universality in the neutral current.

In the context of the Standard Model, $g_{V\ell}$ and $g_{A\ell}$ are related to the effective electroweak mixing angle by:

$$g_{V\ell}/g_{A\ell} = 1 - 4 \sin^2 \theta_{eff}^{lept}. \tag{5}$$

Therefore $\langle P_\tau \rangle$ and A_{pol}^{FB} also provide a precision determination of $\sin^2 \theta_{eff}^{lept}$.

This paper describes a measurement of $\langle P_\tau \rangle$ and A_{pol}^{FB} using the full data sample collected with the OPAL detector at LEP during the period 1990-1995 which corresponds to an integrated luminosity of 151 pb^{-1}. The OPAL measurement of A_{FB}, which is used as input to this analysis, is described in reference[3]. A sample of 144,810 $e^+e^- \to \tau^+\tau^-$ candidate events contained within a fiducial acceptance of $|\cos\theta_{\tau^-}| < 0.90$ is used in the analysis. Most of the selected events (88%) were recorded with the centre-of-mass energy ($\sqrt{s}$) at the peak of the Z^0 resonance and the remainder, referred to as 'off-peak data', were recorded at several distinct $\sqrt{s}$ values within 3 GeV above and below the peak. These new results supersede the measurements reported in Reference [6], which were based on an analysis of a 1990-1994 OPAL data sample that was restricted to the central region of the detector: $|\cos\theta_{\tau^-}| < 0.68$.

The OPAL detector, described in detail in reference [4], consists of a cylindrical magnetic spectrometer embedded in an electromagnetic (ECAL) calorimeter with presampler and a hadronic (HCAL) calorimeter which in turn are enclosed by muon detectors (MUON). A silicon micro-vertex detector, vertex chamber, large volume jet chamber, and z-chambers comprise the central tracking detector (CT). These are contained in a 0.435 T solenoid with magnetic field aligned along the beam axis which defines the z-axis of the detector. The ECAL, consisting of a barrel and two endcap arrays of lead glass blocks, provides complete azimuthal coverage within a polar angle range of $|\cos\theta| < 0.984$. The HCAL and muon detectors are collectively referred to as the 'outer detectors'. The detector covers nearly the entire solid angle and provides full trigger efficiency[5] for $e^+e^- \to \tau^+\tau^-$ events within the acceptance of this analysis.

The $\tau \to e\nu_e\nu_\tau$, $\tau \to \mu\nu_\mu\nu_\tau$, $\tau \to \pi\nu_\tau$, $\tau \to K\ \nu_\tau$, $\tau \to \pi\pi^0\ \nu_\tau$, $\tau \to K\ \pi^0\ \nu_\tau$ and $\tau \to 3\pi^\pm\ \nu_\tau$ decays, representing a combined branching fraction of 83%, are selected and their kinematic properties used to measure the polarization. As nothing in the selection discriminates between charged pions and kaons, the $\tau \to \pi\nu_\tau$ and $\tau \to K\ \nu_\tau$ modes are analysed as a single channel, denoted as $\tau \to \pi\nu_\tau$. The $\tau \to \pi\pi^0\ \nu_\tau$ and $\tau \to K\ \pi^0\ \nu_\tau$ modes are dominated by the $\rho^\pm \to \pi^\pm\pi^0$ and $K^{*\pm} \to K^\pm\pi^0$ resonances, respectively, and are similarly treated as a combined channel denoted as $\tau \to \rho\nu_\tau$. As the $\tau \to 3\pi^\pm\ \nu_\tau$

decays are dominated by the three-prong [2] a_1 resonance, this channel is labelled as $\tau \to a_1 \nu_\tau$. The $\tau \to K\pi\pi\nu_\tau$ and $\tau \to K\ K\pi\nu_\tau$ decay modes are treated as background to the $\tau \to 3\pi^\pm\ \nu_\tau$ channel. The selection criteria for all channels are based on a likelihood technique and have been optimized to reduce the combined statistical and systematic errors.

In order to perform the polarization measurement, the data are fit with linear combinations of left-handed and right-handed Monte Carlo simulated kinematic spectra for each of the five channels. The five decay modes do not all have the same sensitivity to the τ polarization. For the simplest case, the two-body decay of a τ lepton to a spin-zero π meson and τ neutrino, $\tau \to \pi\nu_\tau$, the maximum sensitivity is provided by the energy spectrum of the π. The pure V-A charged current decay of the τ together with angular momentum conservation produces a π momentum preferentially aligned with the helicity of the τ. In the lab frame, this means that a π^- produced from the decay of a right-handed τ^- will, on average, be more energetic than a π^- produced from the decay of a left-handed τ^-. For the leptonic channels, $\tau \to e\nu_e\nu_\tau$ and $\tau \to \mu\nu_\mu\nu_\tau$, the additional unobserved neutrino causes a substantial reduction in polarization sensitivity and the decay of a right-handed τ^- produces, on average, a lower energy charged daughter than a left-handed τ^-. The $\tau \to \rho\nu_\tau$ channel is complicated by the fact that the spin-1 ρ may be produced in two different spin states, the third state being forbidden by angular momentum conservation. The longitudinal state dominates the decay width and is kinematically equivalent to the π channel. In addition there is a significant contribution from the allowed transverse state which is also sensitive to the polarization but in a manner which reduces the polarization sensitivity if only the total visible energy is measured. Much sensitivity is regained by spin-analyzing the $\rho^- \to \pi^-\pi^0$ decay through measurements of the kinematics of the final-state π^- and π^0[7]. The $\tau \to a_1\nu_\tau$ channel, which also involves a spin-1 hadron, is similar to the ρ channel except that the a_1 decays to three pions. As with the $\tau \to \rho\nu_\tau$ channel, sensitivity is optimized by spin-analyzing the $a_1 \to \pi\pi\pi$ decay via measurements of angles between and momenta of the final state pions. The details of the specific variables used for each channel are described Section 4.

The maximum sensitivity for each decay mode, defined as $1/\sqrt{N}\sigma$ where σ is the statistical error on the polarization measurement using N events, is given in Table 1 for P_τ=0.0, assuming that all the information in the decay, apart from the τ direction, is used with full efficiency. A measure of the weight with which a given decay mode ideally contributes to the overall measurement of the polarization is given by that decay mode's sensitivity squared multiplied by its branching ratio. Normalized ideal weights for each decay mode, which are calculated assuming maximum sensitivity and perfect identification efficiency, are also given in Table 1. As can be seen, the $\tau \to \rho\nu_\tau$ and $\tau \to \pi\nu_\tau$ channels are expected to dominate the combined polarization measurement. The actual sensitivity achieved in the experiment for the selected event sample is degraded mainly because of inefficiencies in the process of selecting a sample of decays and by the presence of background in the sample.

The parameters $\langle P_\tau \rangle$ and $A_{\rm pol}^{\rm FB}$ are extracted from the data using a global maximum likelihood fit where the data are described by linear combinations of positive and negative helicity distributions in observables appropriate to each τ decay channel and in θ_{τ^-}. These distributions are obtained from a Monte Carlo simulation in which the τ lepton is assumed to decay according to V-A theory. For those events in which both τ decays have been classified, the analysis explicitly takes into account the τ^+–τ^- longitudinal spin correlation by analysing the event as a whole. In so doing, this also accounts for experimental correlations between the polarization observables introduced by the τ-pair selection and decay mode identification criteria. A beneficial aspect of performing a global fit to all decay modes simultaneously is the automatic inclusion of the correlations between the systematic errors of the different decay modes.

[2] The term 'prong' refers to the track of a charged particle originating from the τ decay vertex.

	$\tau \to e\nu_e\nu_\tau$	$\tau \to \mu\nu_\mu\nu_\tau$	$\tau \to \pi\nu_\tau$	$\tau \to \rho\nu_\tau$	$\tau \to a_1\nu_\tau$ $a_1^\pm \to \pi^\pm\pi^+\pi^-$
Branching ratio	0.18	0.17	0.12	0.25	0.09
Maximum sensitivity	0.22	0.22	0.58	0.49	0.45
Normalized ideal weight	0.06	0.06	0.30	0.44	0.13

Table 1: The branching ratios, maximum sensitivity and normalized ideal weight for the five decay modes used in the analysis. The ideal weight is calculated as the product of the branching ratio and the square of the maximum sensitivity. Presented in the last line of the table is the ideal weight for each channel divided by the sum of the ideal weights of the five channels.

2 Tau Pair Sample

The selection of the particular decays used for the measurement can be viewed as a two stage process where in the first stage a sample of $e^+e^- \to \tau^+\tau^-$ candidates is selected from which samples of $\tau \to e\nu_e\nu_\tau$, $\tau \to \mu\nu_\mu\nu_\tau$, $\tau \to \pi\nu_\tau$, $\tau \to \rho\nu_\tau$ and the three-prong $\tau \to a_1\nu_\tau$ decays are identified in the second stage. The τ-pair selection employs the same basic criteria used in our earlier publications for the barrel region of the detector [6, 8, 9] with slight modifications to allow for an extension of the acceptance into the endcap regions. These are described in detail, along with all aspects of this analysis, in Reference [10]. The general strategy is to identify events characterized by a pair of back-to-back, narrow jets with low particle multiplicity (τ-jet). Background from two-photon processes is then suppressed by requiring that the events have a minimum total visible energy and significant missing transverse momentum when the total energy in the event is low. After removing cosmic ray backgrounds, the events which remain are almost entirely lepton-pairs. Events with high measured energy that are consistent with being $e^+e^- \to e^+e^-$ or $e^+e^- \to \mu^+\mu^-$ are also removed. The polar angle of each τ-jet with respect to the direction of the e^- beam, θ_{jet}, is determined using charged tracks and clusters of deposited energy in the ECAL. Events are selected if the average of $|\cos\theta_{\rm jet}|$ for the two τ-jets, $\overline{|\cos\theta_{\rm jet}|}$, is less than 0.90. The same $\overline{|\cos\theta_{\rm jet}|}$ is used as the estimator for the magnitude of $\cos\theta_{\tau^-}$ in the analysis. Using this selection, a sample of 144,810 events is obtained.

The contributions to the selected events from various physics processes are estimated using a number of Monte Carlo data samples which have approximately ten times the number of events as the data. The $e^+e^- \to \tau^+\tau^-$ signal and $e^+e^- \to \mu^+\mu^-$ background are both modelled using the KORALZ Monte Carlo generator with the TAUOLA decay package [11] and the $e^+e^- \to e^+e^-$ background is estimated using the BHWIDE generator [12]. The residual $e^+e^- \to q\bar{q}$ hadronic background is simulated using the JETSET Monte Carlo [13] with parameters tuned to fit the global event shape distributions of OPAL data [14]. Contributions from non-resonant t-channel two-photon processes ($e^+e^- \to e^+e^-e^+e^-$, $e^+e^- \to e^+e^-\mu^+\mu^-$) are estimated using the generator described in Reference [15] whilst hadronic two-photon processes are modelled using the generator documented in Reference [16]. The potential effects of four-fermion events, including those with hadronic final states, are studied using the generator described in Reference [17]. The response of the OPAL detector to the generated particles in each case is modelled using a simulation program [18] based on the GEANT [19] package. In all cases, the Monte Carlo and real data are treated in an identical manner. Estimates of the $e^+e^- \to \tau^+\tau^-$ selection efficiencies and purities within the different fiducial regions of the analysis are obtained using these Monte Carlo samples and are presented in Table 2.

Region	$\cos\theta$	Efficiency	Purity
Barrel	$\cos\theta \leq 0.72$	93 %	98 %
Overlap	$0.72 < \cos\theta \leq 0.81$	75 %	98 %
Endcap	$0.81 < \cos\theta \leq 0.90$	79 %	97 %

Table 2: τ-pair selection efficiencies and purities for the different fiducial regions of the analysis.

3 Tau Decay Selection

Starting with this sample of τ-pair candidates, each τ-jet in an event is classified as one, and only one, of $\tau \to e\nu_e\nu_\tau$, $\tau \to \mu\nu_\mu\nu_\tau$, $\tau \to \pi\nu_\tau$, $\tau \to \rho\nu_\tau$ or $\tau \to 3\pi^\pm\ \nu_\tau$, or none of these, using a likelihood-based identification procedure. Any event having at least one identified τ-jet is then used in the polarization analysis. From this procedure 129, 902 events contribute to the measurements out of the first-stage selection of 144, 810 events.

Each of the five decay mode selections start with a mode-dependent set of loose cuts which define a sample subsequently processed in a binned likelihood selection[20]. The likelihood selection procedure uses observables which provide discrimination between various decay channels of the τ lepton and non-τ background. The Monte Carlo simulation provides normalized distributions for a set of observables, O_i, for each of the decay modes. These are subsequently used to calculate for each decay channel j, the likelihood, $\ell_i^j(O_i)$, that the measured O_i would be observed. The likelihood that decay mode j produces the measured observables in a given τ-jet is obtained from the product of the likelihoods: $\mathcal{L}(j) = \prod_i \ell_i^j(O_i)$. In order to select decays from mode k, a cut is applied to its relative likelihood, $L(k) = \mathcal{L}(k)/\sum_j \mathcal{L}(j)$. From this definition, $L(k)$ lies between 0 and 1 and the value of the cut is chosen to maximize the product of purity and efficiency. The requirement that decays have large values of $L(k)$ produces a sample with low background normally at the cost of efficiency for selecting mode k decays. In this work, each of the five decay mode selections employ different observables and therefore exploit a different set of likelihoods, $\mathcal{L}(j)$. If a τ-jet is classified in more than one channel after applying the cut to the likelihood, then it is reclassified into the channel having the largest relative likelihood.

Before applying the likelihood selection, fiducial requirements are imposed to remove the small fraction of decays having particles entering regions of the detector which are inadequately modelled by the Monte Carlo simulation. Furthermore, the discrimination between channels is enhanced by dividing the preseleced sample into a set of subsamples according to the detector $|\cos\theta_{\rm jet}|$ region (barrel, overlap or endcap as defined in Table 2) and other τ-jet characteristics, such as the number of electromagnetic clusters in the jet unassociated with tracks.

Approximately 25% of τ leptons decay to ν_τ and a ρ meson, which subsequently decays almost exclusively to a charged and neutral pion. Consequently, much of the discrimination between the $\tau \to \rho\nu_\tau$ and the other decay modes of the τ is achieved by identifying photons from a single π^0 decay which form an invariant mass with a single charged track consistent with the ρ mass, m_ρ. The ECAL observables use a 'maximum entropy' clustering algorithm[21] which is well suited to identifying photons in a τ-jet. A cluster in the barrel (overlap, endcap) region of the detector which is not associated with a charged track is referred to as a 'neutral cluster' if it has an energy of at least 650 MeV (1.25 GeV, 1.0 GeV). When there is only one neutral cluster present in the τ-jet then it is considered as a π^0 candidate. If there are at least two neutral clusters then the invariant mass of the two most energetic clusters forms an observable, $m_{1,2}$, and the invariant mass of this object with the charged track forms the observable referred to as m_ρ. A third invariant mass, m_{jet}, is reconstructed from all neutral clusters and charged tracks in the τ-jet and a fourth, $m_{charged}$, is reconstucted from all charged tracks in the τ-jet. Since 9% of τ leptons decay via $\tau \to \pi 2\pi^0\ \nu_\tau$,

and these can appear as a background in the $\tau \rightarrow \rho\nu_\tau$ channel, a fifth invariant mass, $m_{1-prong}$, is reconstructed from the highest momentum track and the neutral clusters in the τ-jet. If there are more than four neutral clusters, then only the four highest energy clusters are used. These various invariant masses are used as likelihood variables.

The other observables exploited in the likelihood selections are: information from the specific energy loss of the charged track as measured in the central jet chamber (dE/dx); the azimuthal angle between the highest momentum charged track and the presampler cluster closest to that track (ϕ_{pres}); the number of neutral clusters; the ECAL energy associated with the highest momentum track in the τ-jet (E_{ass}); the ratio of E_{ass} to the momentum of the highest momentum track in the τ-jet (E_{ass}/p); the ratio of the ECAL energy of the highest energy cluster to the momentum of the track with the highest momentum in the τ-jet (E_{max}/p); the ratio of the ECAL energy measured in the τ-jet from neutral clusters and clusters associated to tracks to the momentum of the track having the highest momentum in the jet (E_{jet}/p); the energy of the neutral clusters not used in the calculation of m_ρ (E_{resid}); the energy of the neutral clusters used to calculate $m_{1,2}$ ($E_{1,2}$); a variable describing how well the track from the central detector matches a track segment in the muon detectors (CT-MUON); and information from hits measured in HCAL and MUON.

Observable	e	μ	π	ρ	a_1
dE/dx	X	X	X	X	X
ϕ_{pres}		X	X		
No. neutral clusters			X	X	
E_{ass}		X			
E_{ass}/p	X	X	X		X
E_{max}/p					X
E_{jet}/p	X		X	X	X
E_{resid}				X	
$E_{1,2}$				X	X
$m_{1,2}$			X	X	
m_ρ	X	X	X	X	
m_{jet}			X	X	
$m_{charged}$					X
$m_{1-prong}$				X	X
CT-MUON	X	X	X	X	X
HCAL hits		X	X	X	X
MUON hits		X	X	X	X

Table 3: Observables employed in the likelihood selections used to classify the different decay modes. An 'X' indicates that the observable is used in forming the likelihood distribution for the indicated decay mode selection.

The following subsections provide more detail about the likelihood selections for each of the five channels. In particular, the subsections specify for each decay mode: the preselection cuts; the subsamples upon which likelihood selections are separately applied within the three $\cos\theta$ regions of the detector; the observables employed in the likelihood selections, which are summarized in Table 3; efficiencies within the fiducial acceptance after tau pair selection; the amount of cross-contamination from other τ decay modes; and the level of background from non-τ sources. The observables exploited in the likelihood selections are studied and in general are well described by the Monte Carlo simulation. Any differences between the data and simulation of these observables are taken into account in the assessment of the systematic uncertainties on the polarization measurements.

Distributions of two observables characterising each decay mode are plotted in Figures 1(a,b)-5(a,b) as representative indications of the level of agreement between data and the Monte Carlo simulation. The distributions of the likelihoods formed from all observables used in each of the five selections are plotted in Figures 1(c)-5(c). Each of these plots comprise a sum of the various likelihood distributions used for each decay mode selection and further illustrate the adequacy of the detector modelling. The likelihood cut values are optimized separately for each of the various likelihood distributions, and not on the combined distributions plotted here.

3.1 $\tau \rightarrow e\bar{\nu}_e\nu_\tau$ identification

The preselection of the $\tau \rightarrow e\nu_e\nu_\tau$ sample requires, within the τ-jet, that there be no more than three neutral clusters; that no more than three of nine HCAL layers register activity; that no more than three muon chambers register activity; and that there be one or two tracks. If there are two tracks, it is assumed that the higher momentum track is associated with the electron from the τ decay and the lower momentum track is ignored. The observables used to form the likelihoods include: dE/dx, E_{ass}/p, E_{jet}/p, CT-MUON, and m_ρ. The likelihoods in the different regions of the detector are formed for a subsample of τ-jets with the number of neutral clusters equal to zero and for a sample with at least one neutral cluster. Distributions of two of the variables used in this selection, E_{ass}/p, and the pull of the measured dE/dx under an electron hypothesis are shown in Figure 1. The final selection produces a sample of 44,083 candidates with an efficiency of 92% after tau pair selection within the fiducial region and a background of 4.6%. Most of the cross-contamination from τ decays arises from $\tau \rightarrow \pi\nu_\tau$ decays (0.9%) and from $\tau \rightarrow \rho\nu_\tau$ decays (1.3%) along with contributions from a number of other channels (0.8%). The non-τ background is estimated to contribute approximately 1.6%.

3.2 $\tau \rightarrow \mu\nu_\mu\nu_\tau$ identification

The likelihood selection for the $\tau \rightarrow \mu\nu_\mu\nu_\tau$ decays is applied to those τ-jets preselected to have a single charged track, no more than two neutral clusters and a measured track momentum greater than 4% of the beam energy. This sample is divided into subsamples based on information from the outer detectors before forming the likelihoods for the different detector regions. The observables used in this selection include: dE/dx, E_{ass}, E_{ass}/p, ϕ_{pres}, CT-MUON, information from the HCAL and muon chambers, and m_ρ. The distributions of the number of HCAL layers hit in the τ-jet and the number of muon chambers hit for all selected $\tau \rightarrow \mu\nu_\mu\nu_\tau$ decays for both data and Monte Carlo simulation of signal and background are displayed in Figure 2. This selection has an efficiency of 87% after tau pair selection within the fiducial acceptance and background of 3.3% which is heavily dominated by the $\tau \rightarrow \pi\nu_\tau$ decays with some components arising from the $e^+e^- \rightarrow \mu^+\mu^-$ and two-photon processes. This results in the selection of 41,291 decays.

3.3 $\tau \rightarrow \pi\nu_\tau$ identification

The $\tau \rightarrow \pi\nu_\tau$ decay preselection requires that the τ-jet contains one track and that the ratio of the momentum of that track to the beam energy be at least 0.02. Within the different detector regions this sample is divided into subsamples with zero, one or more than one neutral cluster, and subsamples where at least one HCAL layer records hits or where no HCAL layers record hits. For these various samples likelihoods are formed from the following observables: dE/dx, E_{ass}/p, E_{jet}/p, ϕ_{pres}, the number of neutral clusters, CT-MUON, information from the HCAL and muon chambers, $m_{1,2}$, m_ρ, and m_{jet}. Representative distributions of two of the variables important in this analysis are seen in Figure 3 for those τ-jets selected as $\tau \rightarrow \pi\nu_\tau$ candidates: the pull of the measured dE/dx under a pion hypothesis and the number of neutral clusters. A total of 30,440 $\tau \rightarrow \pi\nu_\tau$ candidates

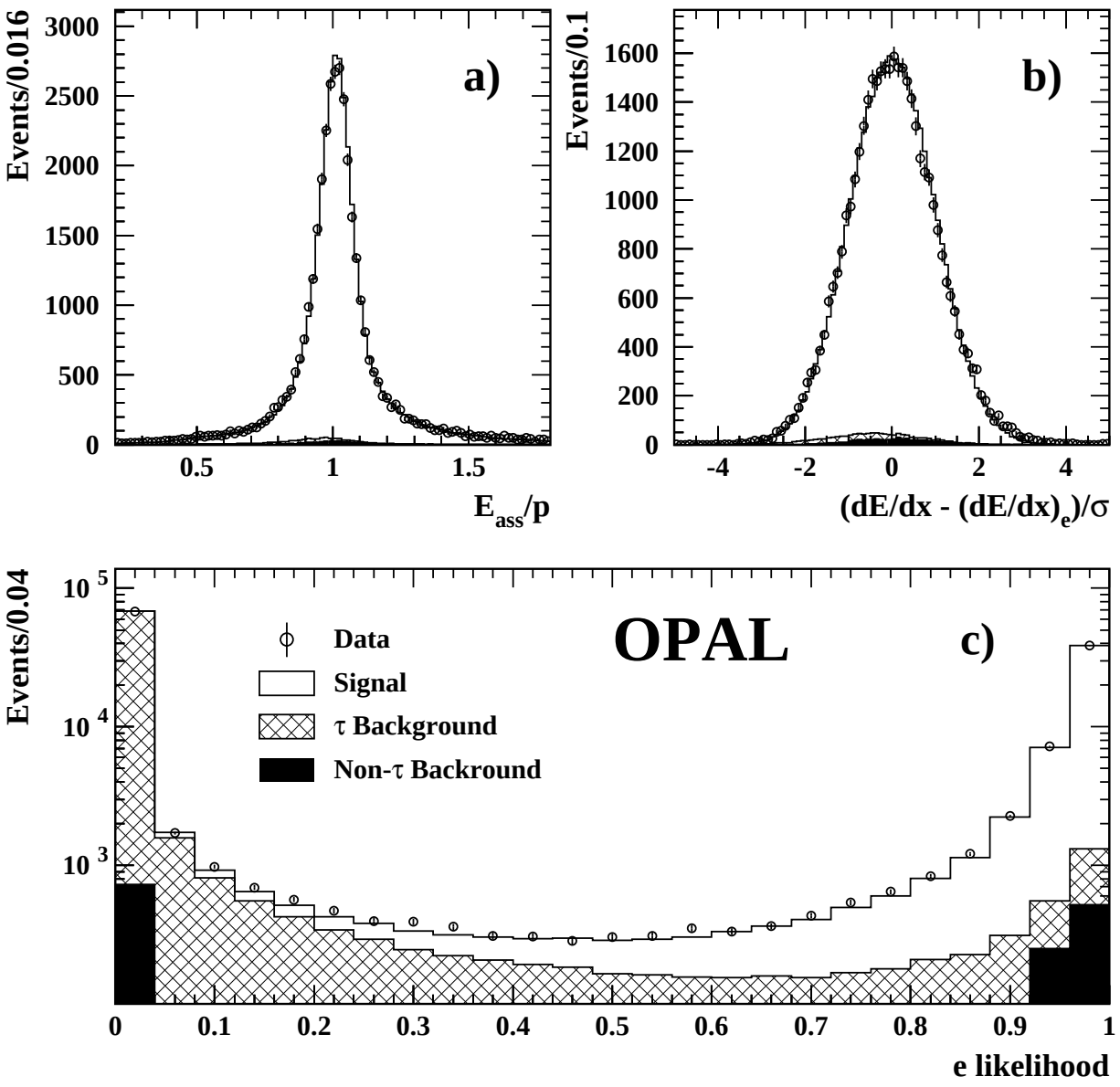

Figure 1: Distributions of (a) E_{ass}/p and (b) pull distribution of measured dE/dx compared to the dE/dx expected under an electron hypothesis for selected $\tau \rightarrow e\nu_e\nu_\tau$candidates. (c) The distribution of likelihoods formed from all observables used in the $\tau \rightarrow e\nu_e\nu_\tau$ selection. In each figure the points with error bars represent the data, the open histogram the $\tau \rightarrow e\nu_e\nu_\tau$ expectation from Monte Carlo, the hatched histogram the cross-contamination from other τ decays and the dark shaded histogram the background from non-τ sources. The distributions include data from all detector regions and subsamples.

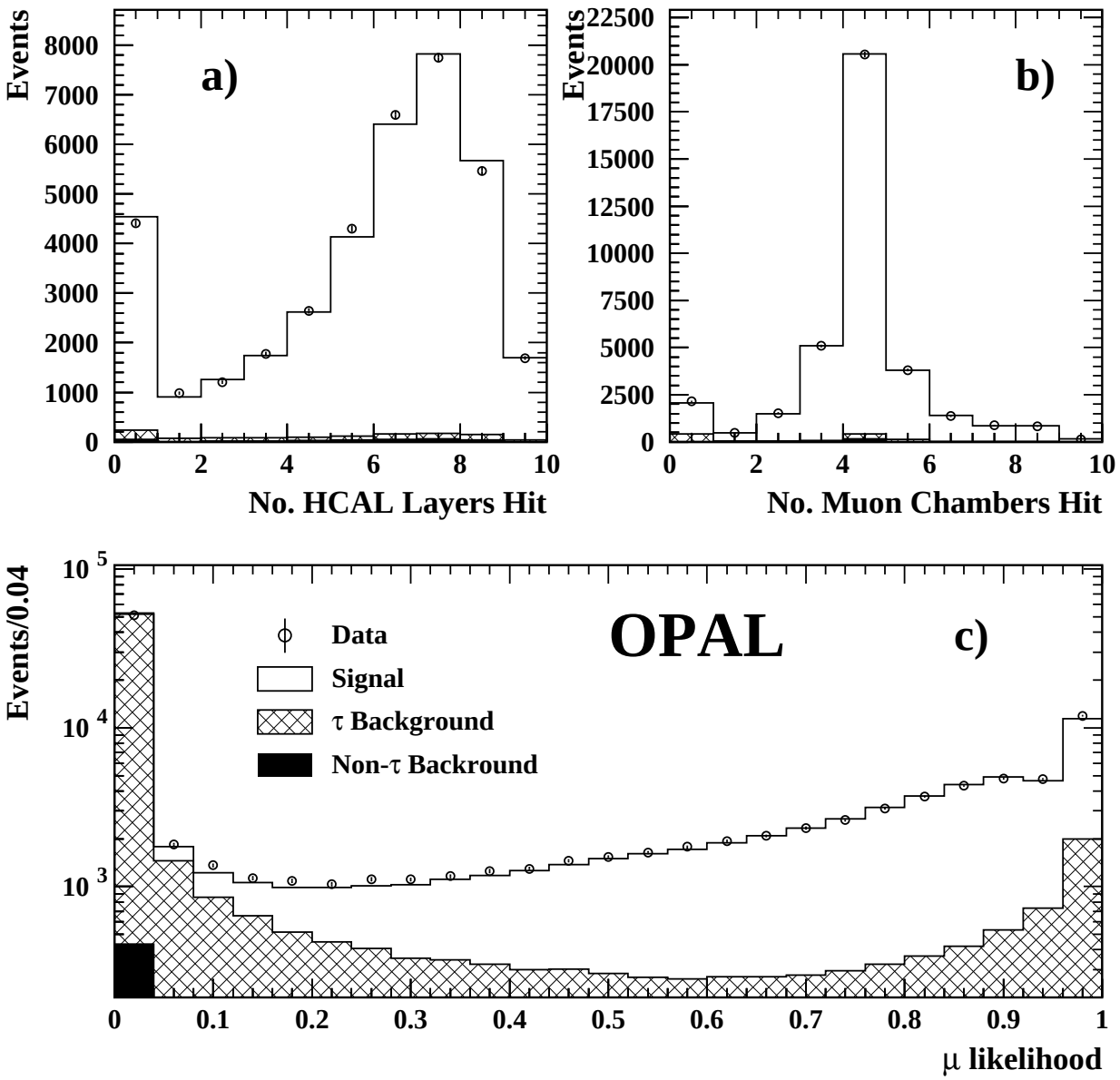

Figure 2: Distributions of (a) the number of HCAL layers hit and (b) the number of muon chambers hit in the $\tau \rightarrow \mu\nu_\mu\nu_\tau$ selected jets. (c) The distribution of likelihoods formed from all observables used in the $\tau \rightarrow \mu\nu_\mu\nu_\tau$ selection. In each figure the points with error bars represent the data, the open histogram the $\tau \rightarrow \mu\nu_\mu\nu_\tau$ expectation from Monte Carlo, the hatched histogram the cross-contamination from other τ decays and the dark shaded histogram the background from non-τ sources. The distributions include data from all detector regions and subsamples.

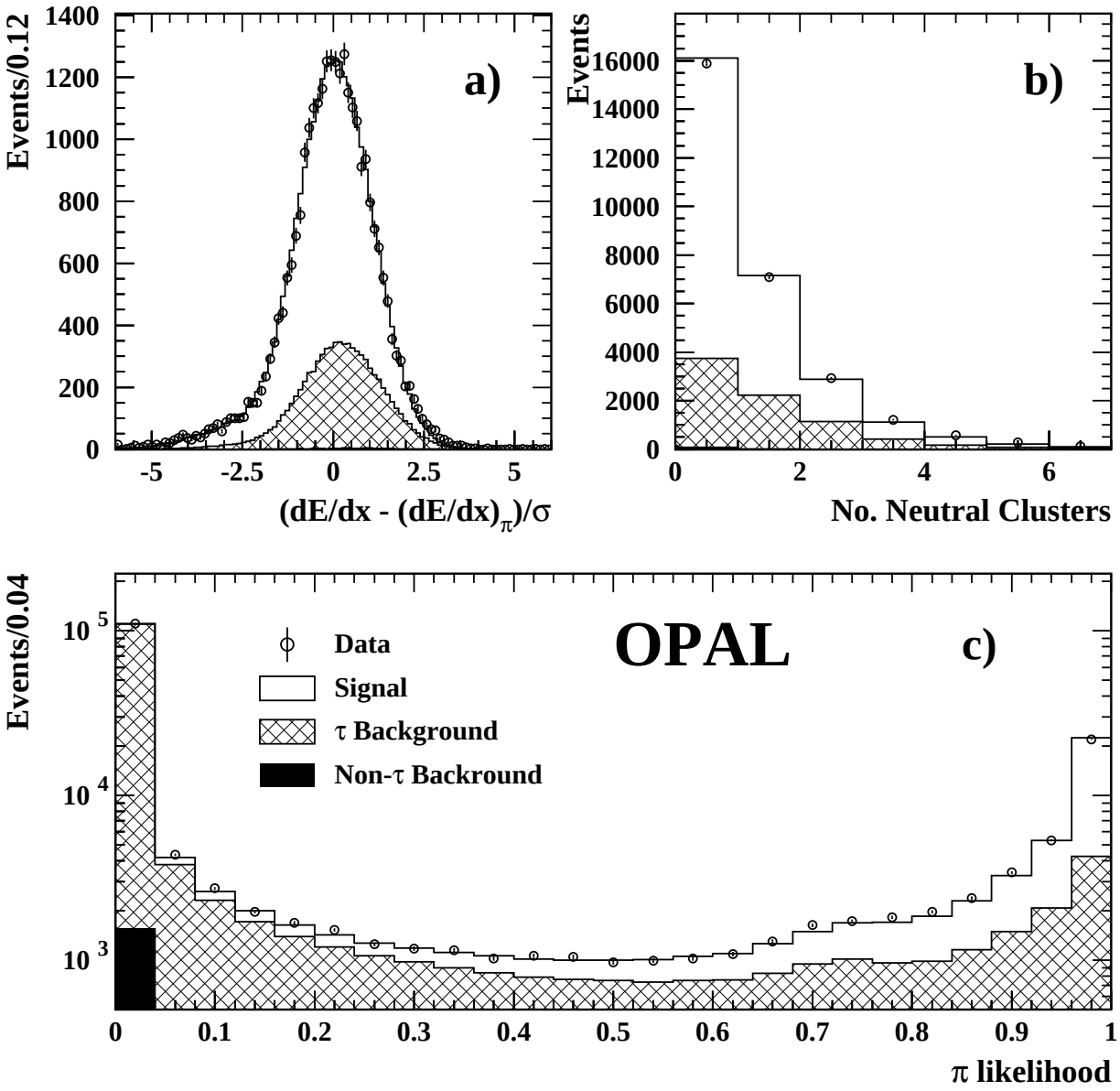

Figure 3: Distributions of (a) pull distribution of measured dE/dx compared to the dE/dx expected under a pion hypothesis and (b) the number of neutral clusters. (c) The distribution of likelihoods formed from all observables used in the $\tau \rightarrow \pi\nu_\tau$ selection. In each figure the points with error bars represent the data, the open histogram the $\tau \rightarrow \pi\nu_\tau$ expectation from Monte Carlo, the hatched histogram the cross-contamination from other τ decays and the dark shaded histogram the background from non-τ sources. The distributions include data from all detector regions and subsamples.

are selected with an efficiency of 75% after tau pair selection within the fiducial region with a background level of 26%. Most of the background arises from the $\tau \rightarrow \rho\nu_\tau$ mode (16%) with the next largest contributions arising from $\tau \rightarrow \mu\nu_\mu\nu_\tau$ (5%) and $\tau \rightarrow a_1\nu_\tau$ (2%). The non-τ background is estimated to contribute approximately 0.2%.

3.4 $\tau \rightarrow \rho\nu_\tau$ identification

The $\tau \rightarrow \rho\nu_\tau$ decay preselection consists solely of the requirement that the τ-jet contains one track. This sample is divided into the subsamples with zero, one or more than one neutral cluster and subsamples where at least one HCAL layer records hits and where no HCAL layers record hits. A number of the observables used to create the likelihood selection are also used for the $\tau \rightarrow \pi\nu_\tau$ likelihood: dE/dx, the number of neutral clusters, E_{jet}/p, CT-MUON, information from the HCAL and muon chambers, $m_{1,2}$, m_ρ, and m_{jet}. Additional observables used to enhance the $\tau \rightarrow \rho\nu_\tau$ selection include: E_{resid}, $E_{1,2}$, and $m_{1-prong}$. The distributions of two of the significant observables used in this selection are displayed in Figure 4 for those τ-jets selected as $\tau \rightarrow \rho\nu_\tau$ candidates: m_ρ and the number of neutral clusters. The analysis selects 67,682 $\tau \rightarrow \rho\nu_\tau$ candidates from the τ-pair sample. Within the polar-angle acceptance, the efficiency is 73%. The background fraction in the $\tau \rightarrow \rho\nu_\tau$ sample is 29% and consists mainly of $\tau \rightarrow \pi(K) \geq 2\pi^0\nu_\tau$ (18%) and $\tau \rightarrow \pi\nu_\tau$ (5%) decays. The non-τ background is estimated to contribute 0.2%.

3.5 $\tau \rightarrow a_1\nu_\tau$ identification

For the $\tau \rightarrow a_1\nu_\tau$ selection we restrict ourselves to the three-prong mode, which has a branching fraction of 9%. It is assumed that all three-pion decays of the τ lepton proceed through the a_1 channel[22]. The $\tau \rightarrow a_1\nu_\tau$ τ-jet is required to have three charged tracks, none of which is identified as a conversion electron. The major contamination for this mode is from $\tau \rightarrow 3\pi \geq 1\pi^0\nu_\tau$ decays. Another potential source of background arises from $e^+e^- \rightarrow e^+e^-$ events containing a conversion, therefore some of the likelihood variables included for the $\tau \rightarrow a_1\nu_\tau$ selection are designed to suppress this contamination. The likelihoods are formed from: dE/dx, E_{ass}/p, E_{jet}/p, E_{max}/p, $E_{1,2}$, CT-MUON, information from the HCAL and muon chambers, $m_{1-prong}$, and $m_{charged}$. The distributions of E_{jet}/p and $m_{charged}$ are plotted in Figure 5 for those τ-jets selected as $\tau \rightarrow a_1\nu_\tau$ candidates for both the data and Monte Carlo simulation of signal and background. The differences between the data and Monte Carlo simulation evident in these plots are adequately described by the systematic uncertainties assessed for this analysis. In particular, the differences between the data and Monte Carlo distributions of $m_{charged}$, Figure 5(b), are well described by the systematic uncertainty ascribed to the modelling of the $\tau \rightarrow a_1\nu_\tau$ decay from the use of different a_1 models[23, 24]. This modelling uncertainty is shown by the lightly shaded region of the histogram in Figure 5(b). The number of selected $\tau \rightarrow a_1\nu_\tau$ candidates is 22,161. The selection efficiency is 77% and the background is 25%, most of which is from $\tau \rightarrow 3\pi \geq 1\pi^0\nu_\tau$ and $\tau \rightarrow K\ \pi^+\pi^-\ \nu_\tau$ decays (20%) and some of which contains residual conversions from $\tau \rightarrow \rho\nu_\tau$ events. The non-tau background in the sample is estimated to be 0.2%.

3.6 Survey of Pair-identification Classes

The fitting approach adopted in this analysis lends itself to a classification of the data in which events are grouped according to the identified decay mode of each of the two τ decays in the event. For example, if in a given event one τ decay is identified as $\tau \rightarrow e\nu_e\nu_\tau$ and the other as $\tau \rightarrow \pi\nu_\tau$ then this event belongs to one pair-identification class, which is denoted as 'π e'. There are 20 such statistically independent classifications including those in which one of the τ decays is identified and the other is not. An example of the latter would be the pair-identification class denoted as

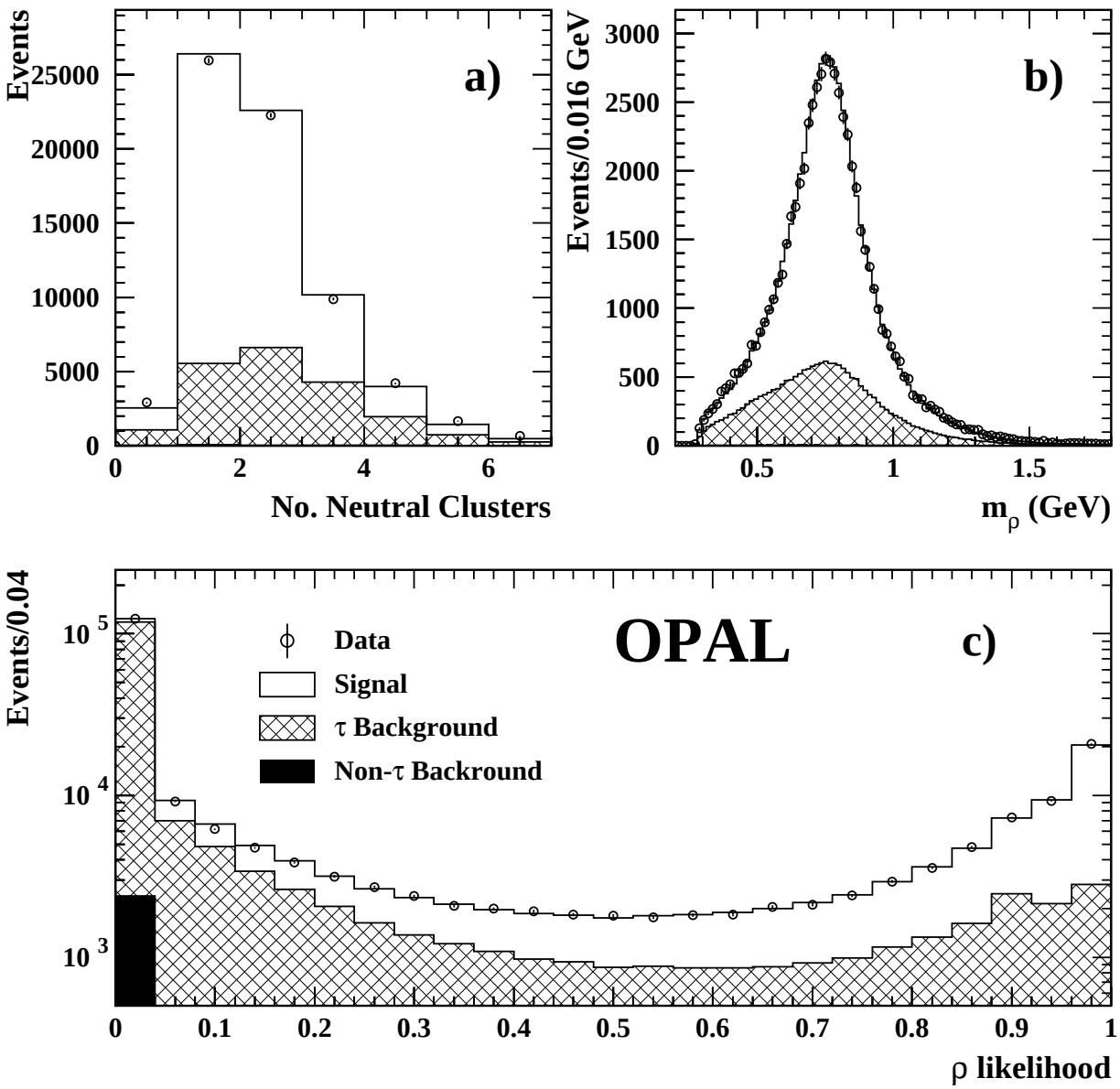

Figure 4: Distributions of (a) the number of neutral clusters for $\tau \rightarrow \rho\nu_\tau$ candidates and (b) the reconstructed ρ mass. (c) The distribution of likelihoods formed from all observables used in the $\tau \rightarrow \rho\nu_\tau$ selection. In each figure the points with error bars represent the data, the open histogram the $\tau \rightarrow \rho\nu_\tau$ expectation from Monte Carlo, the hatched histogram the cross-contamination from other τ decays and the dark shaded histogram the background from non-τ sources. The distributions include data from all detector regions and subsamples.

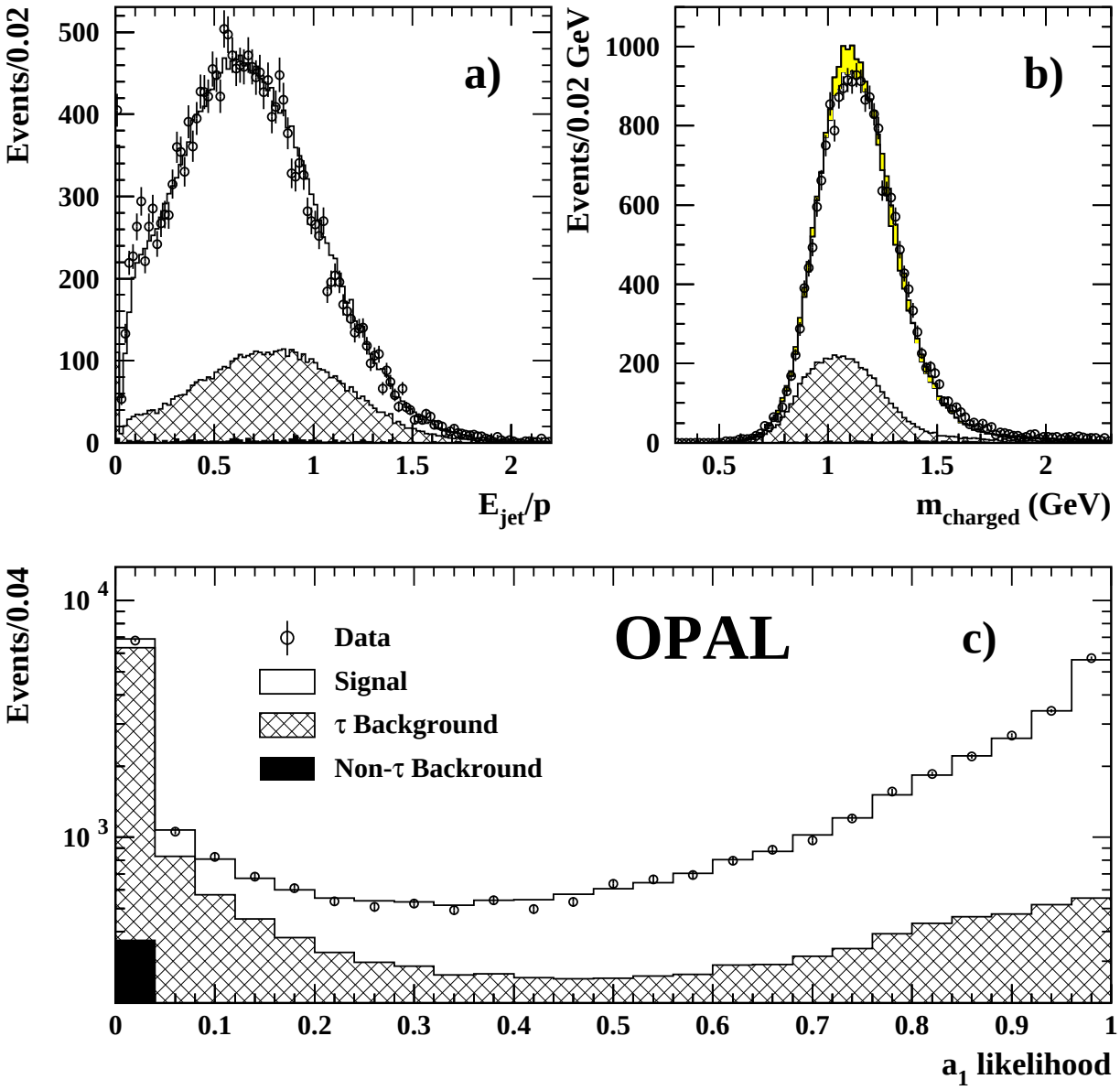

Figure 5: Distributions of (a) the ratio of the total ECAL energy in the τ-jet to the momentum of the track with the highest momentum in the τ-jet and (b) the reconstructed a_1 mass for $\tau \rightarrow a_1 \nu_\tau$ candidates. (c) The distribution of likelihoods formed from all observables used in the $\tau \rightarrow a_1 \nu_\tau$ selection. In each figure the points with error bars represent the data, the open histogram the $\tau \rightarrow a_1 \nu_\tau$ expectation from Monte Carlo, the hatched histogram the cross-contamination from other τ decays and the dark shaded histogram the background from non-τ sources. The lightly shaded region of the histogram in (b) represents the $\tau \rightarrow a_1 \nu_\tau$ decay modelling uncertainty. The distributions include data from all detector regions and subsamples.

'ρ nid' in which one of the τ decays is identified as $\tau \to \rho\nu_\tau$ and the other is not identified. The numbers of data events for each of the 20 possible event pair-identification classes are listed in Table 4. Also shown in the table is the expected number of events from Monte Carlo estimates from τ and non-τ sources, scaled by the absolute luminosity. The good agreement between the data and the expected numbers of events in the different pair-identification classes evident from this table helps validate the overall efficiencies and purities estimated for each class.

	nid	e	μ	π	ρ	a_1
e	12053	3599				
	11793	3584				
μ	11406	6737	2746			
	11211	6601	2707			
π	8382	4786	4302	1669		
	8200	4847	4325	1645		
ρ	18006	10649	10178	7504	8225	
	18186	10782	10230	7460	8482	
a_1	5503	3736	3537	2428	5631	867
	5630	3753	3581	2548	5669	915

Table 4: Number of τ-pair events in each pair-identification class is presented as the first number in each cell. The expected number of events from Monte Carlo estimates using absolute luminosity scaling are shown on the second line. The label 'nid' refers to the case where the τ decay was not identified.

4 Global Fitting Method

For the measurements of $\langle P_\tau \rangle$ and $A_{\rm pol}^{\rm FB}$, the distributions described in Equation 1 cannot be directly measured as it is not possible to determine the τ helicity on an event-by-event basis. Instead, distributions of kinematic variables of the τ decay products which depend on the τ helicity are used. These variables, as well as their distributions, depend on the decay mode analysed[3].

In general, for each τ decay channel, i, the decay distribution depends on a set of kinematic variables, $\vec{\xi_i}$. For positive helicity states the decay distribution can be expressed as $f_i(\vec{\xi_i}) + g_i(\vec{\xi_i})$ whilst for negative helicity states the distribution is $f_i(\vec{\xi_i}) - g_i(\vec{\xi_i})$. Consequently, the measured decay distribution depends linearly on the weighting of the two helicity states, P_τ [25]:

$$\frac{1}{\Gamma_i}\frac{d^n\Gamma_i}{d^n\vec{\xi_i}} = f_i(\vec{\xi_i}) + P_\tau \; g_i(\vec{\xi_i}). \tag{6}$$

For $\tau \to e\nu_e\nu_\tau$, $\tau \to \mu\nu_\mu\nu_\tau$ and $\tau \to \pi\nu_\tau$ decays, $\vec{\xi_i}$ is one dimensional where the relevant kinematic variable (x_e, x_μ or x_π) is the charged particle energy scaled by the beam energy. For $\tau \to e\nu_e\nu_\tau$ decays, the energy measured in the ECAL associated with the τ-jet (x_e) is used, whereas for $\tau \to \mu\nu_\mu\nu_\tau$ and $\tau \to \pi\nu_\tau$ decays, the energy is determined using the momentum of the charged particle measured in the central tracking detector.

For $\tau \to \rho\nu_\tau$ decays, three kinematic variables enter into the polarization analysis: θ^*, the angle of the ρ momentum relative to the τ flight direction in the τ rest frame; ψ, the angle of the charged

[3]Note that the distributions are the same for the τ^+ and τ^- provided that $\langle P_\tau \rangle$ is taken as the τ^- helicity.

pion relative to the ρ flight direction in the ρ rest frame; and m_ρ, the invariant mass of the charged particle under a π^+ hypothesis and the π^0. This spin-analysis of the ρ decay recuperates most of the sensitivity which would otherwise be lost if only the charged pion momentum were used, as discussed in Section 1. These three variables can be converted into a single optimum variable, ω, with no polarization sensitivity loss [7]. The variable ω is defined by $\omega = g/f = (R_+ - R_-)/(R_+ + R_-)$ where R_+ and R_- are the population densities of positive and negative helicity τ lepton decays, respectively, which are functions of θ^*, ψ and m_ρ [7].

The $\tau \to a_1 \nu_\tau$ channel is more complicated because the a_1 decays into three pions. Six observables are used in order to improve the sensitivity in the $\tau \to a_1 \nu_\tau$ channel[7]: the angle (θ^*) between the a_1 and τ momenta in the τ rest frame, the angle (ψ) between the perpendicular to the a_1 decay plane and the a_1 flight direction in the rest frame of the a_1, the angle (γ) in the a_1 rest frame between the unlike-sign pion momentum in the a_1 rest frame and the a_1 flight direction projected into the a_1 decay plane, the 3π-invariant mass, and the two $\pi^+\pi^-$ mass combinations present in the $a_1^\pm \to \pi^\pm\pi^+\pi^-$ decay. The distribution of the invariant mass of the three charged particles assuming them all to be pions, shown in Figure 5b, demonstrates that agreement between the data and simulation of this quantity is reasonable within the uncertainties of the modelling of the $\tau \to a_1 \nu_\tau$ decay. The Monte Carlo distribution depends on the mass and width of the a_1 as defined within the framework of a particular model of $\tau \to a_1 \nu_\tau$ decay[23] and allowance in the assignment of systematic errors is made for $\tau \to a_1 \nu_\tau$ model dependence. As with the $\tau \to \rho \nu_\tau$, these observables are converted into a single optimum variable, ω, which this time depends on the population densities of positive and negative helicity τ lepton decays which are functions of the six variables mentioned above.

The joint distributions of the τ-pair production and decay can be expressed in the improved Born approximation as:

$$\begin{aligned}\frac{d^3\sigma_{ij}}{d\cos\theta_{\tau^-}\, dx_i\, dx_j} &= \tfrac{3}{16}\sigma_{ij} \sum_{\lambda=\pm1} [(1+\cos^2\theta_{\tau^-} + \tfrac{8}{3} A_{FB} \cos\theta_{\tau^-}) + \\ &\lambda(\langle P_\tau \rangle (1+\cos^2\theta_{\tau^-}) + \tfrac{8}{3} A_{pol}^{FB} \cos\theta_{\tau^-})] \times \\ &[F_i(x_i, |\cos\theta_{\tau^-}|) + \lambda G_i(x_i, |\cos\theta_{\tau^-}|)][F_j(x_j, |\cos\theta_{\tau^-}|) + \lambda G_j(x_j, |\cos\theta_{\tau^-}|)],\end{aligned} \tag{7}$$

where σ_{ij} is the cross-section to produce an $e^+e^- \to \tau^+\tau^-$ event in which one τ decays via channel i and the other via channel j. The first two lines of Equation 7 refer to the production of the τ-pairs and the third line to the τ decays. The summation over λ indicates that the summation is over positive and negative helicities. The symbol x_i represents the kinematic variable corresponding to channel i: x_e, x_μ, x_π, ω_ρ or ω_{a_1}. The decay distributions for positive-helicity τ leptons are given by $F_i + G_i$ whereas the decay distributions for negative-helicity τ leptons are given by $F_i - G_i$. F_i and G_i represent functions of x_i and $|\cos\theta_{\tau^-}|$ after including the effects of the decay mode identification procedure, detector response and radiation. The simulation of the underlying detector measurements that go into each of the observables used in the analysis, such as track momentum and ECAL cluster energies and positions, is checked and corrected if necessary, using various control samples as discussed below. Equation 7 includes the correlation between the decay distributions of the two τ leptons when analysing events in which both τ decay channels are identified.

A binned maximum likelihood fit is performed to simultaneously extract $\langle P_\tau \rangle$ and A_{pol}^{FB} by fitting the linear combination of the positive and negative helicity Monte Carlo distributions to the data. The values of x_i, x_j and $\cos\theta_{\tau^-}$ for each event are calculated and a histogram, binned[4] in x_i, x_j and $\cos\theta_{\tau^-}$, is then filled for each $\sqrt{s}$. A value for $\cos\theta_{\tau^-}$ of the event is determined from $|\cos\theta_{jet}|$ and the sign of the charge of the identified τ decay. A separate set of histograms exists for each combination of decay channel pairs. If only one τ decay is identified, then only bins in x_i

[4] There are ten bins in $\cos\theta_{\tau^-}$ and ten bins in each of x_e, x_μ, x_π, ω_ρ, and ω_{a_1}.

and $\cos\theta_{\tau^-}$ are filled. The same procedure is performed for the Monte Carlo with a separate set of histograms filled for the positive and negative helicity τ leptons binned in x_i, x_j and $|\cos\theta_{\tau^-}|$. This provides the product $[F_i + \lambda G_i][F_j + \lambda G_j]$ as a function of $|\cos\theta_{\tau^-}|$ in the Monte Carlo, which uses the fact that the detector is symmetric in $\cos\theta_{\tau^-}$. As a consequence, the forward and backward hemispheres use the same Monte Carlo sample. Therefore, the correlations in the Monte Carlo samples result in a reduced Monte Carlo statistical error on $\mathrm{A}_{\mathrm{pol}}^{\mathrm{FB}}$.

The Monte Carlo statistics are taken into account in the likelihood fit in the manner described in Reference [26]. In order to identify the contribution to the total error arising from the data statistical error only, a second fit is performed which does not take into account the Monte Carlo statistical errors. The Monte Carlo statistical error is taken to be the quadratic difference between the error from the two fits and quoted as part of the systematic error of the polarization results.

The effects on the measured polarization arising from misidentified τ decays are modelled by the Monte Carlo simulation. The helicity dependence of the misidentified decays is automatically taken into account in the product $[F_i + \lambda G_i][F_j + \lambda G_j]$. Contributions from the small non-τ background are estimated using Monte Carlo simulations of distributions in the relevant kinematic variables. As there is no helicity dependence in this background, these distributions are added to the linear combination of the right-handed and left-handed τ decay Monte Carlo distributions to form the complete reference distributions used in the fit.

The fit also depends on A_{FB} for which the measured value in the $\mathrm{Z}^0 \to \tau^+\tau^-$ channel [3] at the appropriate $\sqrt{\mathrm{s}}$ is used. Separate distributions for the different values of $\sqrt{\mathrm{s}}$ are used in order to account for the A_{FB} dependence but a single fit for $\langle P_\tau \rangle$ and $\mathrm{A}_{\mathrm{pol}}^{\mathrm{FB}}$ is performed. Although there are potential dependences of the observables in the analysis on the exact value of $\sqrt{\mathrm{s}}$ at which the data were collected, the use of beam-energy normalized observables renders the analysis relatively insensitive to such effects. However, in order to further reduce any such dependences, the data collected with $\sqrt{\mathrm{s}}$ below 90.7 GeV and above 91.7 GeV are analysed using Monte Carlo samples generated at fixed centre-of-mass energies where most of the off-peak data were collected. The majority of the off-peak data were collected with values of $\sqrt{\mathrm{s}}$ within 0.2 GeV of the values used in the Monte Carlo generation.

5 Polarization Fit Results

The results of the global fit are:

$$\begin{aligned} \langle P_\tau \rangle &= (-14.10 \pm 0.73 \pm 0.55)\% \\ \mathrm{A}_{\mathrm{pol}}^{\mathrm{FB}} &= (-10.55 \pm 0.76 \pm 0.25)\%, \end{aligned} \tag{8}$$

where the first error is statistical and the second systematic. The correlation between the two parameters, including both statistical and systematic correlations, is less than 0.03. Although this result uses data collected over a number of different centre-of-mass energies, to a very good approximation it can be treated as though it were all collected at a single effective centre-of-mass energy of 91.30 GeV. Whereas the systematic error evaluation is discussed in detail in Sections 6 and 7, this section will outline a number of studies which validate the internal consistency of the results.

The global fit technique has been checked with independent fits to each channel, the results of which are presented in Table 5. The weighted average of $\langle P_\tau \rangle$ for these fit results differs slightly from that obtained from the global fit. This difference is consistent with expected statistical fluctuations when comparing results obtained using the global fit which takes into account correlations and a weighted average which does not. The values obtained for the five different channels are also consistent with each other and the global fit values. A χ^2 of 4.9 for four degrees of freedom is found

when comparing the five values of $\langle P_\tau \rangle$ to the value from the global fit and 2.1 for four degrees of freedom when comparing the values of A_{pol}^{FB} .

	$\tau \to e\nu_e\nu_\tau$	$\tau \to \mu\nu_\mu\nu_\tau$	$\tau \to \pi\nu_\tau$	$\tau \to \rho\nu_\tau$	$\tau \to a_1\nu_\tau$
Sample size	44,083	41,291	30,440	67,682	22,161
Efficiency	92%	87%	75%	73%	77%
Background	4.6%	3.3%	26%	29%	25%
$\langle P_\tau \rangle$ (%)	-18.7 ± 2.5	-16.3 ± 2.7	-13.8 ± 1.2	-13.3 ± 1.1	-11.6 ± 2.8
A_{pol}^{FB} (%)	-8.9 ± 2.6	-10.6 ± 2.8	-11.5 ± 1.3	-10.6 ± 1.1	-7.1 ± 2.8

Table 5: The number of decays in the sample, selection efficiency after tau pair selection within the fiducial acceptance and background for each decay mode analysed. Results of independent fits for the individual decay modes are also presented where the error quoted represents that arising from the data statistics only. The measurements from the individual channels are correlated and therefore should not be combined in a simple average.

An indication of the validity of the Monte Carlo simulation of the kinematic variables used in the fit, as well as the assumed efficiencies and purities, is provided by the one-dimensional distributions of the relevant kinematic variables for the five channels. The distributions combined over all $\cos\theta_{\tau^-}$ bins are shown in Figure 6 for both the data and Monte Carlo. The χ^2 comparison between data and Monte Carlo simulation for these distributions, shown on each plot, suggests that the efficiencies and background are adequately simulated in these distributions for all modes. Also shown are the Monte Carlo distributions of the variables for positive and negative helicity τ lepton decays and their sum including non-τ background, assuming the value of $\langle P_\tau \rangle$ quoted in Equation 8. These plots illustrate the sensitivities of the measured kinematic distributions to the polarization.

Another tool for investigating the internal consistency of the analysis is afforded by comparing the fitted values of $\langle P_\tau \rangle$ and A_{pol}^{FB} for each event pair-identification class as defined in Section 3.6. These comparisons are shown in Figures 7 and 8 where the results of the fits both in graphical and numeric form for each pair-identification class in the global analysis are presented. The χ^2 probability describing the statistical significance of the different values from the global fit value[5] for $\langle P_\tau \rangle$ and A_{pol}^{FB} indicate internal consistency. The ideogram formed from the sum of the individual Gaussians is overlayed on the data points. This illustrates that for both $\langle P_\tau \rangle$ and A_{pol}^{FB} the spread in fit values for the different pair-identification classes is symmetric about the global fit value and the peak is consistent with that value.

High statistics internal consistency is also examined for events which have both τ decays classified compared to those where only one τ decay is classified. These comparisons, also shown in Figures 7 and 8, indicate strong overall internal consistency of the results.

As a further check on the validity of the fit, the results of fits for P_τ performed independently in ten bins of $\cos\theta_{\tau^-}$ are shown in Figure 9. For the fit in a particular $\cos\theta_{\tau^-}$ bin, an expression analogous to that shown in Equation 7 is used in which $(\langle P_\tau \rangle\ (1+\cos^2\theta_{\tau^-}) + \frac{8}{3} A_{pol}^{FB} \cos\theta_{\tau^-})$ in the second line of Equation 7 is replaced by $(P_\tau(1+\cos^2\theta_{\tau^-} + \frac{8}{3} A_{FB} \cos\theta_{\tau^-}))$. This substitution uses Equation 2. Overlaying these points is a curve which represents the expectation value of P_τ as a function of $\cos\theta_{\tau^-}$ from Equation 2 where the values of the $\langle P_\tau \rangle$ and A_{pol}^{FB} from the global fit of Equation 8 are used. The results of the ten independent fits are in good agreement with the expectations from the global fit: the χ^2 is 6.8 for eight degrees of freedom when comparing the ten

[5]These are calculated using data statitistical errors only.

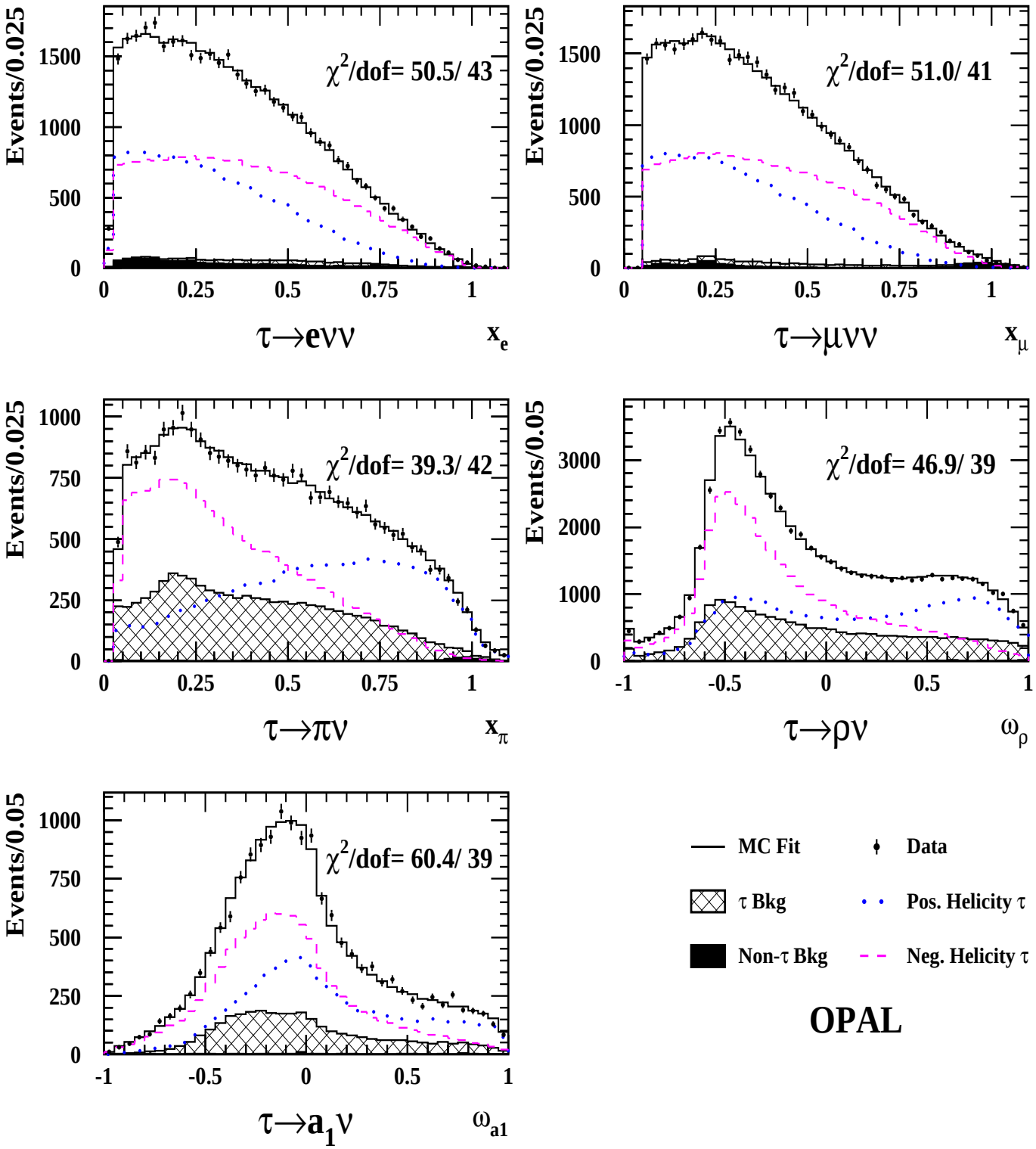

Figure 6: Distributions in the kinematic variables used in the fits as discussed in the text for the $\tau\to e\nu_e\nu_\tau$, $\tau\to\mu\nu_\mu\nu_\tau$, $\tau\to\pi\nu_\tau$, $\tau\to\rho\nu_\tau$, and $\tau\to a_1\nu_\tau$ channels where the data, shown by points with error bars, are integrated over the whole $\cos\theta_{\tau^-}$ range. Overlaying these distributions are Monte Carlo distributions for the positive (dotted line) and negative (dashed line) helicity τ leptons and for their sum including background, assuming a value of $\langle P_\tau\rangle = -14.10\%$ as reported in the text. The hatched histogram represent the Monte Carlo expectations of contributions from cross-contamination from other τ decays and the dark shaded histogram the background from non-τ sources. The level of agreement between the data and Monte Carlo distributions is quantified by quoting the χ^2 and the number of degrees of freedom.

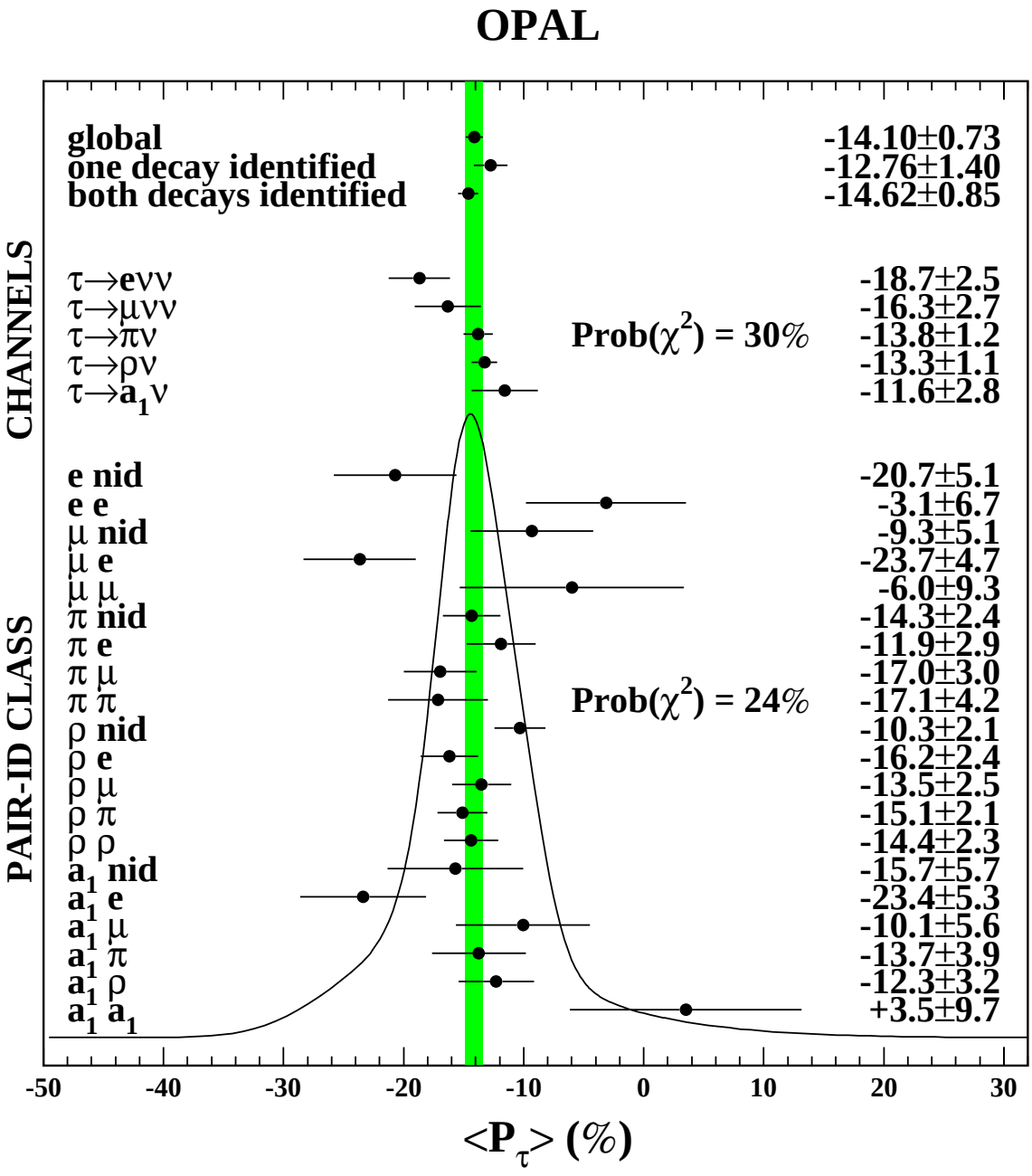

Figure 7: Internal consistency of the $\langle P_\tau \rangle$ results investigated as a function of the number of τ decays classified in the event and by pair-identification class. The ideogram formed from the sum of the individual Gaussians is superimposed on the pair-identification results. The χ^2 probabilities of the spreads about the global fit value are shown for each subsample and show good internal consistency in all cases. The label 'nid' refers to the case where the τ decay is not identified.

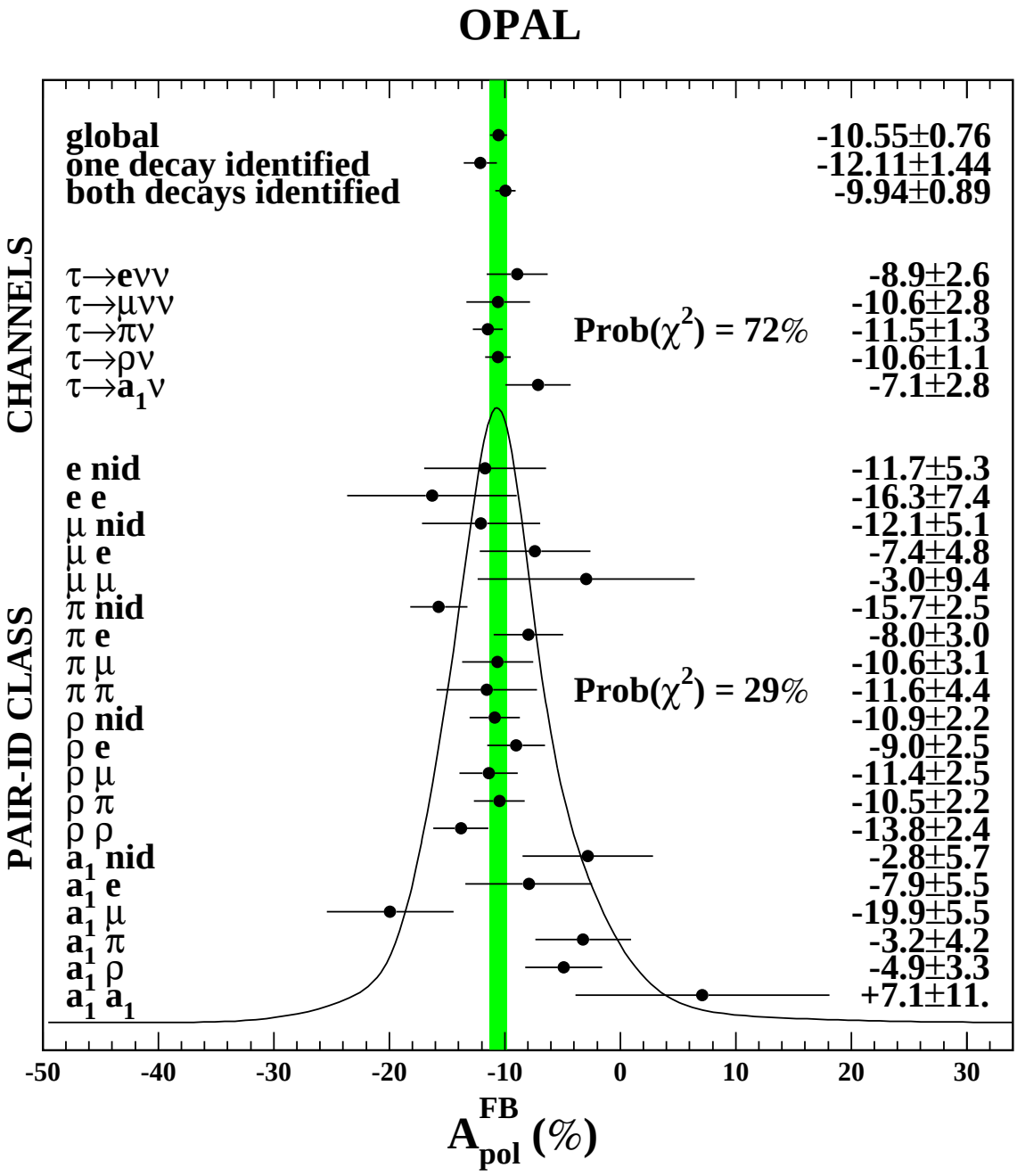

Figure 8: Internal consistency of the A_{pol}^{FB} results investigated as a function of the number of τ decays classified in the event and by pair-identification class. The ideogram formed from the sum of the individual Gaussians is superimposed on the pair-identification class results. The χ^2 probabilities of the spreads about the global fit value are shown for each subsample and show good internal consistency in all cases. The label 'nid' refers to the case where the τ decay is not identified.

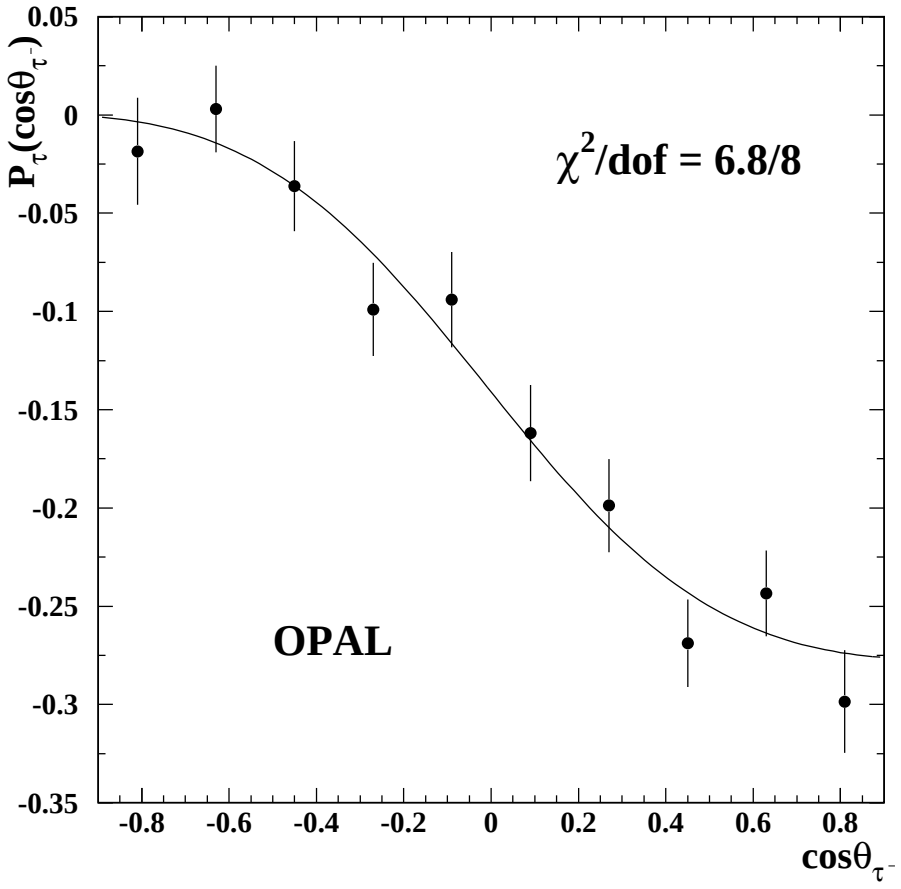

Figure 9: Tau polarization, $\langle P_\tau \rangle$, as a function of $\cos\theta_{\tau^-}$. The data points represent the P_τ values obtained from a global fit to all channels in each $\cos\theta_{\tau^-}$ bin. The error bars represent data statistical errors only. The curve represents the expectation from the global fit result: $\langle P_\tau \rangle = -14.10\%$ and $\mathrm{A}_{\mathrm{pol}}^{\mathrm{FB}} = -10.55\%$ as reported in the text.

values of P_τ to the expected value from the global fit where only the data statistics are included in calculating the χ^2.

Because a non-negligible amount of data is collected off-peak, measurements of $\langle P_\tau \rangle$ and $\mathrm{A}_{\mathrm{pol}}^{\mathrm{FB}}$ are also performed separately for data collected at centre-of-mass energies below, on and above the Z^0 resonance peak. The three statistically independent measurements are quoted in Table 6. In order to compare the consistency between these measurements, they are all converted into measurements of $\mathcal{A}_\tau$ or $\mathcal{A}_\mathrm{e}$ using the technique described in Section 8. These asymmetry values, also quoted in Table 6, are consistent with each other. Because the conversions from $\langle P_\tau \rangle$ to $\mathcal{A}_\tau$ and from $\mathrm{A}_{\mathrm{pol}}^{\mathrm{FB}}$ to $\mathcal{A}_\mathrm{e}$ assume the Standard Model centre-of-mass dependence of $\langle P_\tau \rangle$ and $\mathrm{A}_{\mathrm{pol}}^{\mathrm{FB}}$, the agreement between the $\mathcal{A}_\tau$ and $\mathcal{A}_\mathrm{e}$ values in Table 6 indicates that the data are consistent with the Standard Model expectations for this centre-of-mass dependence.

$\sqrt{s}$ (GeV)	$\langle P_\tau \rangle$ (%)	A_{pol}^{FB} (%)	$\mathcal{A}_\tau$	$\mathcal{A}_e$
89.5 ± 0.2	-15.9 ± 3.3	-8.0 ± 3.4	0.186 ± 0.039	0.125 ± 0.040
91.25 ± 0.05	-13.52 ± 0.78	-10.52 ± 0.81	0.1393 ± 0.0081	0.145 ± 0.011
93.0 ± 0.2	-18.1 ± 2.9	-11.3 ± 3.0	0.176 ± 0.028	0.146 ± 0.040

Table 6: Global fit values of $\langle P_\tau \rangle$ and A_{pol}^{FB} for data collected below, on and above the Z^0 resonance peak. The luminosity weighted values of $\sqrt{s}$ are quoted in the first column where the error reflects the spread in $\sqrt{s}$ values of the data combined in each fit. The neutral current asymmetry parameters with their statistical errors, based on the data collected at the different centre-of-mass energies, are also quoted.

6 Detector Related Systematic Errors

Because the Monte Carlo simulation provides the positive and negative helicity reference distributions in the fit and is used for the likelihood selections, it is necessary that the detector response be accurately modelled and a systematic error attributed to each relevant discrepency between the detector simulation and data. The approach taken in this analysis is to determine the accuracy of the detector modelling of specific measured quantities, to vary that quantity in the simulation, and then to propogate the influence of that variation through a complete analysis of all decay modes.

High purity control samples of muons with momenta of approximately 45 GeV from $e^+e^- \to \mu^+\mu^-$ events are used to determine corrections to the simulation of the momentum scale and resolution of the central tracking detector. The systematic uncertainties of these corrections yield a transverse momentum scale uncertainty of 0.14% in the barrel region of the detector with higher values of 0.8% and 0.4% in the overlap and endcap regions, respectively. Studies of measurements of the mass of the K_S^0 from $K_S^0 \to \pi^+\pi^-$ in $e^+e^- \to q\bar{q}$ hadronic events provide a calibration point of the momentum scale at the lower energies. The tracking resolution corrections are cross-checked at lower energies using the transverse momentum distributions in $e^+e^- \to e^+e^-\mu^+\mu^-$ two-photon processes. Modelling uncertainties of the $\cos\theta$ measurements of the tracks in the tracking chambers are evaluated independently of transverse momentum using back-to-back tracks from $e^+e^- \to \mu^+\mu^-$ events and cross-checked with other detectors such as the presampler. Pure samples of electrons with energies of approximately 45 GeV from $e^+e^- \to e^+e^-$ events are used to determine corrections to the simulation of the energy scale and resolution of the ECAL. These corrections were evolved to lower energies using the ratio of the deposited energy to measured momentum for electrons in $e^+e^- \to e^+e^-e^+e^-$ two-photon processes and in high purity $\tau \to e\nu_e\nu_\tau$ samples. Uncertainties of 0.3% on the ECAL energy scale in the barrel, 0.6% in the overlap and 0.4% in the endcap are estimated from these studies. The one standard deviation errors on the energy scale and momentum scale are used in assessing the systematic errors on $\langle P_\tau \rangle$ and A_{pol}^{FB} from an analysis using rescaled energy and momenta which takes into account the correlations between channels. In a similar manner, systematic errors associated with uncertainties in the parameters used to describe the resolutions of the ECAL and tracking detector resolution are also assigned.

High purity muon and $\tau \to \rho\nu_\tau$ samples are used to correct the modelling of the response of the HCAL and muon chambers to muons and hadrons. Variation of the magnitude of these corrections is used to assess the systematic error on $\langle P_\tau \rangle$ and A_{pol}^{FB} associated with this modelling. Correct modelling of the dE/dx measurement is achieved by studying the response of the tracking detector to high purity $\tau \to e\nu_e\nu_\tau$ and $\tau \to \mu\nu_\mu\nu_\tau$ samples selected without using dE/dx information. The corrections applied to the dE/dx simulation are changed in order to assess the sensitivity of $\langle P_\tau \rangle$ and A_{pol}^{FB} to this modelling. The effects of uncertainties in the amount of material in the central detector,

which potentially affects the photon conversion background in the a_1 channel, were studied and found to have a negligible influence on the polarization measurement.

The uncertainty in the modelling of the lateral spread of the electromagnetic and hadronic showers in the ECAL contributes significantly to the overall systematic error. This is particularly relevant for the separation of the $\tau \to \pi\nu_\tau$ and $\tau \to \rho\nu_\tau$ samples. The influence of these uncertainties on the polarization measurement is estimated by varying the thresholds in the cluster definitions for the simulation and from the cluster position and position resolution uncertainties. The ECAL cluster position resolution is also sensitive to the lateral shower spread in the ECAL. A control sample of electrons is used to improve the modelling of the ECAL cluster position resolution and to assign uncertainties to this modelling by varying the magnitude of the corrections applied to the simulation. Further checks of this class of systematic error were performed by studying the stability of the results from the likelihood selection when excluding individual observables related to showering.

There is also a potential systematic error on A_{pol}^{FB} related to charge mis-assignment, which in OPAL is negligible.

The contributions to the uncertainty on $\langle P_\tau \rangle$ and A_{pol}^{FB} from these various sources are shown in Table 7. These are obtained by varying the associated detector-level quantities, such as corrections to the simulated momentum or HCAL layers hit, and redoing the analysis from the tau pair selection, through the calculation of physics observables such as m_ρ and decay classification, to the global fit for $\langle P_\tau \rangle$ and A_{pol}^{FB}. The table includes the systematic errors for each of the five channels in addition to the errors for the global analysis. The systematic correlations between channels are automatically accounted for in this analysis and fully incorporated into the systematic error quoted for the global fit results.

	$\Delta\langle P_\tau \rangle$ and ΔA_{pol}^{FB}											
	e		μ		π		ρ		a_1		Global fit	
Momentum scale/resolution	0.4	0.2	2.1	0.1	0.8	0.1	0.3	0.1	0.4	0.2	0.24	0.13
ECAL scale/resolution	3.2	0.1	0.2	0.1	0.2	–	1.1	0.2	0.3	0.1	0.17	0.11
HCAL/MUON modelling	0.1	–	1.1	0.1	0.5	0.1	–	–	–	–	0.13	0.05
dE/dx errors	0.6	0.1	0.3	0.1	0.3	0.1	0.1	0.1	0.3	0.1	0.12	0.08
Shower modelling in ECAL	0.6	0.1	0.2	0.1	0.4	0.1	0.5	0.2	0.4	0.1	0.25	0.10
Branching ratios	0.1	–	0.1	–	0.2	–	0.2	–	0.2	0.1	0.11	0.02
$\tau \to a_1\nu_\tau$ modelling	–	–	–	–	–	–	0.4	–	0.5	0.1	0.22	0.02
$\tau \to 3\pi \geq 1\pi^0\nu_\tau$ modelling	–	–	–	–	–	–	–	–	1.2	0.1	0.11	0.04
A_{FB}	–	0.2	–	–	–	–	–	–	–	–	0.03	0.02
Decay radiation	–	–	–	–	–	–	–	–	0.1	–	0.01	0.01
Monte Carlo statistics	0.7	0.2	0.8	0.3	0.3	0.1	0.3	0.1	0.8	0.2	0.22	0.10
total	3.4	0.4	2.6	0.4	1.2	0.2	1.3	0.3	1.7	0.3	0.55	0.25

Table 7: Tabulation of systematic errors contributing to $\langle P_\tau \rangle$ and A_{pol}^{FB} when these asymmetries are expressed as a percentage, for each of the five decay modes analysed and the global fit. In each column the error on $\langle P_\tau \rangle$ is given first followed by that on A_{pol}^{FB}. Systematic error correlations between the five channels are fully incorporated into the systematic error on the global result. In the second to sixth columns a dash indicates that the listed effect contributes less than 0.05%.

7 Physics Related Systematic Errors

Another class of systematic uncertainties relates to our knowledge of τ production and decay. In this category are the errors on measured branching ratios of the different τ decay modes. The branching ratios used are obtained from the averages of the measurements in Reference [28]. The error on $\langle P_\tau \rangle$ and A_{pol}^{FB} associated with the uncertainty of each branching ratio is estimated by varying the value used in the global analysis by ± 1 standard deviation about its average value.

The uncertainty in the modelling of the $\tau \rightarrow a_1 \nu_\tau$ decay introduces systematic errors both in the $\tau \rightarrow a_1 \nu_\tau$ channel and in the $\tau \rightarrow \rho \nu_\tau$ channel where the $\tau \rightarrow a_1 \nu_\tau$ decays represent a significant fraction of the selected decays. Two contributions to the $\tau \rightarrow a_1 \nu_\tau$ modelling uncertainty are considered: one being the uncertainty in the mass and width of the a_1 as obtained from Reference [29] and the other obtained by comparing two independent theoretical treatments of the $\tau \rightarrow a_1 \nu_\tau$ decay [23, 24, 30].

In addition to the $\tau \rightarrow a_1 \nu_\tau$ modelling uncertainty, the modelling of the $\tau \rightarrow 3\pi \geq 1\pi^0 \nu_\tau$ decays potentially introduces a further uncertainty in the analysis of the $\tau \rightarrow a_1 \nu_\tau$ channel. This is studied using the Monte Carlo simulation by varying the $\tau^- \rightarrow \omega \pi^-$ contribution to the $\tau \rightarrow 3\pi\pi^0 \nu_\tau$ mode and by flipping the helicity of the τ in the $\tau \rightarrow 3\pi > 1\pi^0 \nu_\tau$ decays. The latter effect is found to contribute negligibly to the systematic error.

Two smaller sources of error also fall into this general category of systematic error: the error associated with the measured value of A_{FB} for $e^+e^- \rightarrow \tau^+\tau^-$ events which is obtained from Reference [3] and the uncertainty of the simulation of radiation. Both initial and final state radiation are sufficiently well modelled in the Monte Carlo and contribute negligibly to the systematic uncertainties. The simulation of radiation in the decay of the τ is treated in the same manner as is described in Reference [8]. The uncertainty in the modelling of radiation in all modes is found to contribute negligibly to the overall systematic error.

The contributions arising from the various systematic errors are summarized in Table 7 for each of the independent analyses and for the global analysis which takes into account the correlations between channels.

Because the fits also depend on our knowledge of the non-τ sources of background, there are potential systematic errors arising from the uncertainty in the production cross-sections. Varying the cross-sections within their errors in the reference distributions used in the fits makes negligible changes to the polarization results. To cross-check the contributions of non-τ background, distributions of acoplanarity, acolinearity and total event transverse momentum, which would have regions enhanced in the two-photon, $e^+e^- \rightarrow \mu^+\mu^-$, and $e^+e^- \rightarrow e^+e^-$ events, were studied and show no indication of uncontrolled sources of non-tau background. The samples of two photon and $e^+e^- \rightarrow e^+e^-$ events are further enhanced by examining off-peak data where, again, there is no evidence of problems with these sources. Another cross-check is provided by studing the numbers of events in the different pair-identification classes, where, once more, there is no indication that additional systematic errors associated with non-tau backgrounds need to be quoted beyond those included in accounting for the detector response related systematic errors.

8 Neutral Current Asymmetry Parameter Results

The polarization measurements quoted in Equation 8 are consistent with our previous measurements [8] but with a total error that has been reduced by nearly a factor of two. The results are also consistent with those published by other LEP collaborations [31, 32, 33].

As discussed in the introduction the Standard Model gives predictions for $\langle P_\tau \rangle$ and A_{pol}^{FB} in terms of $\sqrt{s}$, the mass and width of the Z^0 , $g_{V\ell}$ and $g_{A\ell}$. The connection is made through the

neutral current asymmetry parameters as defined in Equation 4. The measurements of $\langle P_\tau \rangle$ and A_{pol}^{FB} are dominated by the Z^0 propagator but also include small contributions from the photon propagator, photon-Z^0 interference and photonic radiative corrections. ZFITTER [27] provides the $\sqrt{s}$ dependent non-Z^0 propagator contributions to $\langle P_\tau \rangle$ and A_{pol}^{FB} as well as higher-order corrections to Equation 2 within the context of the Standard Model. This allows the measured parameters to be expressed in terms of $\mathcal{A}_\tau$ and $\mathcal{A}_e$:

$$\begin{aligned} \mathcal{A}_\tau &= 0.1456 \pm 0.0076 \pm 0.0057, \\ \mathcal{A}_e &= 0.1454 \pm 0.0108 \pm 0.0036. \end{aligned}$$

Within the context of the Standard Model these results can be interpreted as measurements of:

$$\begin{aligned} g_{V\tau}/g_{A\tau} &= 0.0732 \pm 0.0048, \\ g_{Ve}/g_{Ae} &= 0.0731 \pm 0.0057, \end{aligned}$$

where the statistical and systematic errors of $\mathcal{A}_\tau$ and $\mathcal{A}_e$ are added in quadrature before calculating the errors on $g_{V\tau}/g_{A\tau}$ and g_{Ve}/g_{Ae}. The agreement between these two values indicates that the data are consistent with the hypothesis of lepton universality. This test of lepton universality can be expressed as a measurement of the ratio of the tau vector to axial vector couplings to the electron vector to axial vector couplings:

$$\frac{g_{V\tau}/g_{A\tau}}{g_{Ve}/g_{Ae}} = 1.00 \pm 0.10.$$

If universality is assumed, these data can be averaged and expressed as a single leptonic asymmetry parameter:

$$\mathcal{A}_\ell = 0.1455 \pm 0.0073.$$

Using Equations 4 and 5, this result can be expressed as:

$$\sin^2\theta_{eff}^{lept} = 0.23172 \pm 0.00092.$$

This measurement of $\sin^2\theta_{eff}^{lept}$ is of similar precision to other individual measurements at LEP using various techniques and is in agreement with the value of $\sin^2\theta_{eff}^{lept}$ obtained from a Standard Model fit to all LEP electroweak data, including previous measurements of the τ polarization[34]. It is also consistent with a determination of $\sin^2\theta_{eff}^{lept}$ from a measurement of A_{LR} by the SLD collaboration[35].

9 Combined Lineshape and Asymmetry Results from OPAL

The tau polarization results can be combined with the measurements from the leptonic partial widths and forward-backward asymmetries published by OPAL[3] to provide measurements of $g_{V\ell}$ and $g_{A\ell}$ for electrons, muons and τ leptons separately. While $\mathcal{A}_\tau$ and $\mathcal{A}_e$ provide measurements of $g_{V\ell}/g_{A\ell}$ for the τ and electron, the leptonic partial widths of the Z^0 provide measurements of ${g_{V\ell}}^2 + {g_{A\ell}}^2$ for all three lepton flavours. The forward-backward asymmetries determine $(g_{Ve}g_{V\ell})/(g_{Ae}g_{A\ell})$ for electrons, muons and τ leptons yielding additional information about $g_{V\tau}/g_{A\tau}$ and g_{Ve}/g_{Ae}, and provide the only means of measuring $g_{V\mu}/g_{A\mu}$ at LEP.

The OPAL measurements of the hadronic and leptonic cross-sections and leptonic forward-backward asymmetries at the Z^0 pole are summarized in terms of nine model-independent Z^0 parameters as defined in Reference [3]: the mass (M_Z), width (Γ_Z) and the hadronic pole cross-section

M_{Z} (GeV)	91.1858 ± 0.0030
Γ_{Z} (GeV)	2.4948 ± 0.0041
σ^0_{h} (nb)	41.501 ± 0.055
R_{e}	20.902 ± 0.084
R_μ	20.811 ± 0.058
R_τ	20.832 ± 0.091
$A^{0,\mathrm{e}}_{\mathrm{FB}}$	0.0089 ± 0.0044
$A^{0,\mu}_{\mathrm{FB}}$	0.0159 ± 0.0023
$A^{0,\tau}_{\mathrm{FB}}$	0.0145 ± 0.0030
$\mathcal{A}_{\mathrm{e}}$	0.1454 ± 0.0114
$\mathcal{A}_\tau$	0.1456 ± 0.0095

Table 8: The first nine parameters are the result of fitting the model-independent Z^0 parameters to the measured cross-sections and asymmetries measured by OPAL [3]. The parameters $\mathcal{A}_{\mathrm{e}}$ and $\mathcal{A}_\tau$ are the result of the current analysis of the τ polarization.

	M_{Z}	Γ_{Z}	σ^0_{h}	R_{e}	R_μ	R_τ	$A^{0,\mathrm{e}}_{\mathrm{FB}}$	$A^{0,\mu}_{\mathrm{FB}}$	$A^{0,\tau}_{\mathrm{FB}}$	$\mathcal{A}_{\mathrm{e}}$	$\mathcal{A}_\tau$
M_{Z}	1.00	0.05	0.03	0.11	0.00	0.00	−0.05	0.08	0.06	0.00	0.00
Γ_{Z}	0.05	1.00	−0.35	0.01	0.02	0.01	0.00	0.00	0.00	0.00	0.00
σ^0_{h}	0.03	−0.35	1.00	0.15	0.22	0.14	0.01	0.01	0.01	0.00	0.00
R_{e}	0.11	0.01	0.15	1.00	0.09	0.04	−0.20	0.03	0.02	0.00	0.00
R_μ	0.00	0.02	0.22	0.09	1.00	0.06	0.00	0.01	0.00	0.00	0.00
R_τ	0.00	0.01	0.14	0.04	0.06	1.00	0.00	0.00	0.01	0.00	0.00
$A^{0,\mathrm{e}}_{\mathrm{FB}}$	−0.05	0.00	0.01	−0.20	0.00	0.00	1.00	−0.02	−0.01	0.00	0.00
$A^{0,\mu}_{\mathrm{FB}}$	0.08	0.00	0.01	0.03	0.01	0.00	−0.02	1.00	0.02	0.00	0.00
$A^{0,\tau}_{\mathrm{FB}}$	0.06	0.00	0.01	0.02	0.00	0.01	−0.01	0.02	1.00	0.00	0.01
$\mathcal{A}_{\mathrm{e}}$	0.00	0.00	0.00	0.00	0.00	0.00	0.00	0.00	0.00	1.00	0.03
$\mathcal{A}_\tau$	0.00	0.00	0.00	0.00	0.00	0.00	0.00	0.00	0.01	0.03	1.00

Table 9: Error correlation matrix for the 11 parameters entering the fit for the leptonic couplings presented in Table 8.

	Without lepton universality	With lepton universality	Standard Model prediction
$\mathcal{A}_{\rm e}$	0.1375 ± 0.0093		
$\mathcal{A}_{\mu}$	0.154 ± 0.024		
$\mathcal{A}_{\tau}$	0.1449 ± 0.0091		
$\mathcal{A}_{\ell}$		0.1424 ± 0.0054	$0.1450^{+0.0030}_{-0.0084}$

Table 10: The leptonic neutral current asymmetry parameters obtained from a fit to the Z^0 parameters given in Table 8. In the last column is given the value of the parameter calculated in the context of the Standard Model assuming the parameter variations given in the text.

	$\mathcal{A}_{\rm e}$	$\mathcal{A}_{\mu}$	$\mathcal{A}_{\tau}$
$\mathcal{A}_{\rm e}$	1.00	-0.43	-0.09
$\mathcal{A}_{\mu}$	-0.43	1.00	0.04
$\mathcal{A}_{\tau}$	-0.09	0.04	1.00

Table 11: Error correlation matrix for the measurements of the leptonic neutral current asymmetry parameters, which are presented in Table 10.

($\sigma^0_{\rm h}$) of the Z^0 resonance; the ratios of the hadronic to leptonic partial widths ($R_{\rm e}$,R_{μ} and R_{τ}); and the leptonic pole forward-backward asymmetries ($A^{0,\mu}_{\rm FB}$,$A^{0,\mu}_{\rm FB}$ and $A^{0,\tau}_{\rm FB}$). The values of these nine parameters, together with the polarization asymmetries reported here, are displayed in Table 8 and the error correlation matrix in Table 9.

Information from the tau polarization and forward-backward asymmety measurements can be combined to provide measurements of the three leptonic neutral current asymmetry parameters, $\mathcal{A}_{\rm e}$, $\mathcal{A}_{\mu}$ and $\mathcal{A}_{\tau}$. These and their error correlation maxtrix are shown in Tables 10 and 11. The results for the three lepton species are consistent with each other and agree well with the prediction of the Standard Model[6] which is also shown in Table 10. Assuming lepton unversality,

$$\mathcal{A}_{\ell} = 0.1424 \pm 0.054.$$

This can also be expressed in terms of the effective weak mixing angle:

$$\sin^2 \theta^{\rm lept}_{\rm eff} = 0.23211 \pm 0.00068.$$

The eleven model-independent Z^0 parameters listed in Table 8 can also be used to determine the neutral current vector and axial-vector couplings for each lepton species. The results and the error correlation matrix are given in Tables 12 and 13 and are illustrated in Figure 10. Some of

[6]The Standard Model calculations require the full specification of the fundamental Standard Model parameters. The main parameters are the masses of the Z^0 boson ($M_{\rm Z}$), the top quark ($m_{\rm t}$) and the Higgs boson ($m_{\rm H}$), and the strong and electromagnetic coupling constants, $\alpha_{\rm s}$ and α. As in Reference [3] the calculation of Standard Model predictions use the following values and ranges: $M_{\rm Z} = 91.1856 \pm 0.0030$ GeV, $m_{\rm t} = 175 \pm 5$ GeV, $m_{\rm H} = 150^{+850}_{-60}$ GeV, $\alpha_{\rm s} = 0.119 \pm 0.002$, and $\alpha({M_{\rm Z}}^2)^{-1} = 128.886 \pm 0.090$. The choice of these parameter values and ranges is discussed in Reference [3].

the couplings have up to approximately 50% correlations between their errors. Evident from these results is the universality of the coupling constants which can be quantified in terms of the ratios of the couplings:

$$\frac{g_{\mathrm{A}\mu}}{g_{\mathrm{Ae}}} = 1.0011 \pm 0.0025, \quad \frac{g_{\mathrm{A}\tau}}{g_{\mathrm{Ae}}} = 1.0021 \pm 0.0029, \quad \frac{g_{\mathrm{A}\tau}}{g_{\mathrm{A}\mu}} = 1.0009 \pm 0.0027,$$
$$\frac{g_{\mathrm{V}\mu}}{g_{\mathrm{Ve}}} = 1.12 \pm^{0.24}_{0.21}, \qquad \frac{g_{\mathrm{V}\tau}}{g_{\mathrm{Ve}}} = 1.06 \pm^{0.11}_{0.10}, \qquad \frac{g_{\mathrm{V}\tau}}{g_{\mathrm{V}\mu}} = 0.94 \pm^{0.18}_{0.14}.$$

The axial-vector couplings of the different lepton species are found to be the same at the 0.3% level. The errors on the inter-species ratios of the vector couplings are much larger because of the smaller size of the vector couplings themselves, but within this reduced sensitivity, again no significant differences are observed. These errors have been significantly reduced by adding information from the tau polarization to the lineshape and forward-backward asymmetry measurements[3].

Combining the values of the coupling constants from the different lepton species under the assumption of lepton universality yields the values

$$g_{\mathrm{A}\ell} = -0.50089 \pm 0.00045, \quad g_{\mathrm{V}\ell} = -0.0358 \pm 0.0014.$$

where the correlation between $g_{\mathrm{A}\ell}$ and $g_{\mathrm{V}\ell}$ is -19%, which is approximately the same as the -21% correlation between $g_{\mathrm{A}\ell}$ and $\sin^2\theta^{\mathrm{lept}}_{\mathrm{eff}}$. These are in good agreement with the predictions of the Standard Model, which are included in Table 12.

	Without lepton universality	With lepton universality	Standard Model prediction
g_{Ae}	-0.50062 ± 0.00062		
$g_{\mathrm{A}\mu}$	-0.50117 ± 0.00099		
$g_{\mathrm{A}\tau}$	-0.50165 ± 0.00124		
$g_{\mathrm{A}\ell}$		-0.50089 ± 0.00045	$-0.50130^{+0.00047}_{-0.00013}$
g_{Ve}	-0.0346 ± 0.0023		
$g_{\mathrm{V}\mu}$	$-0.0388^{+0.0060}_{-0.0064}$		
$g_{\mathrm{V}\tau}$	-0.0365 ± 0.0023		
$g_{\mathrm{V}\ell}$		-0.0358 ± 0.0014	$-0.0365^{+0.0022}_{-0.0008}$

Table 12: Axial-vector and vector couplings obtained from a fit to the parameter set given in Table 8. In the last column we give the values of the couplings calculated in the context of the Standard Model assuming the parameter variations given in the text.

10 Summary

Measurements of $\langle P_\tau \rangle$ and $\mathrm{A}^{\mathrm{FB}}_{\mathrm{pol}}$ have been made using the complete LEP I data sample of OPAL. The results are based on a simultaneous analysis of $\tau \to \mathrm{e}\nu_e\nu_\tau$, $\tau \to \mu\nu_\mu\nu_\tau$, $\tau \to \pi\nu_\tau$, $\tau \to \rho\nu_\tau$ and $\tau \to \mathrm{a}_1\nu_\tau$ decays from a sample of $144,810$ $\mathrm{e^+e^-} \to \tau^+\tau^-$ candidates collected over nearly the entire solid angle of the OPAL detector. Under the assumption that the τ lepton decays according to

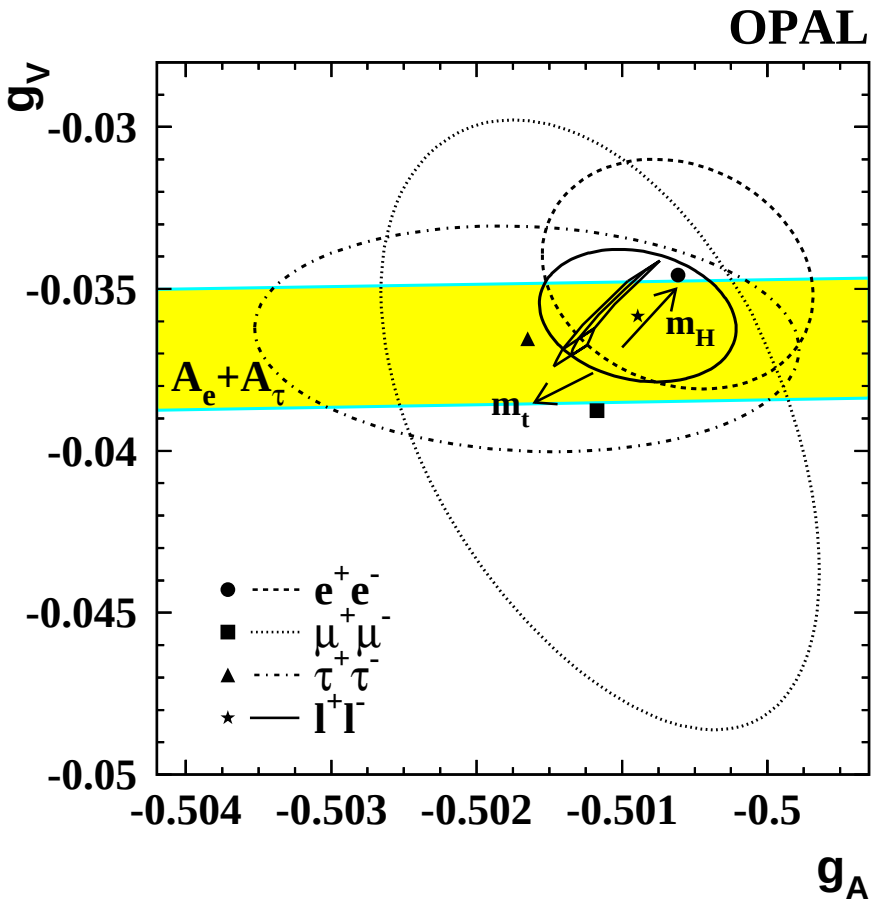

Figure 10: $g_{V\ell}$ *vs* $g_{A\ell}$ as determined from the OPAL measurements of the leptonic partial widths of the Z^0 , forward-backward asymmetries and tau polarization measurements. The ellipses represent the 68% confidence level contours in the $g_{V\ell}$-$g_{A\ell}$ plane for each lepton species separately (dotted and dashed) and for all leptons assuming universality (solid). The central values are displayed at the centre of the ellipses as a circle, square, triangle and star for electrons, muons, tau leptons and all leptons under universality, respectively. The Standard Model prediction is shown with variations from the top quark mass (170 to 180 GeV) and Higgs mass (90 to 1000 GeV) indicated. The OPAL tau polarization measurements of $\mathcal{A}_\tau$ and $\mathcal{A}_e$ constrain $g_{V\ell}$ and $g_{A\ell}$ to lie in the shaded region at the 68% confidence level.

	g_{Ae}	$g_{\mathrm{A}\mu}$	$g_{\mathrm{A}\tau}$	g_{Ve}	$g_{\mathrm{V}\mu}$	$g_{\mathrm{V}\tau}$
g_{Ae}	1.00	$-.17$	$-.13$	$-.19$	.07	.01
$g_{\mathrm{A}\mu}$	$-.17$	1.00	.29	.19	$-.46$	$-.03$
$g_{\mathrm{A}\tau}$	$-.13$	.29	1.00	$-.04$	.03	$-.08$
g_{Ve}	$-.19$	.19	$-.04$	1.00	$-.45$	$-.04$
$g_{\mathrm{V}\mu}$	.07	$-.46$	.03	$-.45$	1.00	.03
$g_{\mathrm{V}\tau}$	.01	$-.03$	$-.08$	$-.04$	.03	1.00

Table 13: Error correlation matrix for the measurements of the axial vector and vector couplings, without assuming lepton universality, which are presented in Table 12.

V−A theory, the average τ polarization near $\sqrt{s} = \mathrm{M_Z}$ is measured to be $\langle P_\tau \rangle = (-14.10 \pm 0.73 \pm 0.55)\%$ and the τ polarization forward-backward asymmetry to be $\mathrm{A_{pol}^{FB}} = (-10.55 \pm 0.76 \pm 0.25)\%$. Taking into account the small effects of the photon propagator, photon-Z^0 interference and photonic radiative corrections, these results can be expressed in terms of the lepton neutral current asymmetry parameters:

$$\begin{aligned} \mathcal{A}_\tau &= 0.1456 \pm 0.0076 \pm 0.0057, \\ \mathcal{A}_\mathrm{e} &= 0.1454 \pm 0.0108 \pm 0.0036. \end{aligned}$$

These measurements are consistent with the hypothesis of lepton universality and combine to give $\mathcal{A}_\ell = 0.1455 \pm 0.0073$. Within the context of the Standard Model this corresponds to $\sin^2\theta_{\mathrm{eff}}^{\mathrm{lept}} = 0.23172 \pm 0.00092$.

Combining the information from the tau polarization results with the results of the other OPAL neutral current measurements yields values for the vector and axial-vector couplings which are the same for all lepton species and gives

$$g_{\mathrm{A}\ell} = -0.50089 \pm 0.00045, \quad g_{\mathrm{V}\ell} = -0.0358 \pm 0.0014.$$

Expressing these results in terms of the electroweak mixing angle gives

$$\sin^2\theta_{\mathrm{eff}}^{\mathrm{lept}} = 0.23211 \pm 0.00068.$$

This is consistent with the Standard Model and with the current world average value[34].

Acknowledgements

We particularly wish to thank the SL Division for the efficient operation of the LEP accelerator at all energies and for their continuing close cooperation with our experimental group. We thank our colleagues from CEA, DAPNIA/SPP, CE-Saclay for their efforts over the years on the time-of-flight and trigger systems which we continue to use. In addition to the support staff at our own institutions we are pleased to acknowledge the
Department of Energy, USA,
National Science Foundation, USA,
Particle Physics and Astronomy Research Council, UK,

Natural Sciences and Engineering Research Council, Canada,
Israel Science Foundation, administered by the Israel Academy of Science and Humanities,
Minerva Gesellschaft,
Benoziyo Center for High Energy Physics,
Japanese Ministry of Education, Science and Culture (the Monbusho) and a grant under the Monbusho International Science Research Program,
Japanese Society for the Promotion of Science (JSPS),
German Israeli Bi-national Science Foundation (GIF),
Bundesministerium für Bildung und Forschung, Germany,
National Research Council of Canada,
Research Corporation, USA,
Hungarian Foundation for Scientific Research, OTKA T-029328, T023793 and OTKA F-023259.

References

[1] D. Bardin, M. Grunewald and G. Passarino, "Precision calculation project report," hep-ph/9902452.

[2] S. Jadach and Z. Wąs in *Z Physics at LEP1*, CERN 89-08, edited by G. Altarelli *et al.*, Vol. 1 (1989) 235.

[3] OPAL Collab., M.Z. Akrawy *et al.*, Phys. Lett. **B240** (1990) 497;
OPAL Collab., G. Alexander *et al.*, Z. Phys. **C52** (1991) 175;
OPAL Collab., P.D. Acton *et al.*, Z. Phys. **C58** (1993) 219;
OPAL Collab., R. Akers *et al.*, Z. Phys. **C61** (1994) 19;
OPAL Collab., *Precise Determination of the Z Resonance Parameters at LEP: 'Zedometry'*, CERN-EP-2000-148, Submitted to Eur. Phys. J. C. to be published.

[4] OPAL Collab., K. Ahmet *et al.*, Nucl. Inst. and Meth. **A305** (1991) 275.

[5] OPAL Collab., K. Arignon *et al.*, Nucl. Inst. and Meth. **A313** (1992) 103.

[6] OPAL Collab., G. Alexander *et al.*, Z. Phys. **C72** (1996) 365.
The OPAL combined results from the 1996 paper are: $\mathcal{A}_\tau = 0.134 \pm 0.009 \pm 0.010$, $\mathcal{A}_\mathrm{e} = 0.129 \pm 0.014 \pm 0.005$, $\sin^2\theta^{\mathrm{lept}}_{\mathrm{eff}} = 0.2334 \pm 0.0012$.

[7] M.Davier *et al.*, Phys. Lett. **B306** (1993) 411;
A.Rougé, Proceeding of the Workshop on Tau Lepton Physics, M.Davier and B.Jean-Marie Editors, Edition Frontières (1991) 213.

[8] OPAL Collab., R. Akers *et al.*, Z. Phys. **C65** (1995) 1.

[9] OPAL Collab., G. Alexander *et al.*, Phys. Lett. **B266** (1991) 201.

[10] K. Graham, 'Precision Determination of the Electroweak Mixing Angle and Test of Neutral Current Universality from the Tau Polarization Measurements at OPAL', University of Victoria PhD Thesis (in preparation). Will be available from the National Archives of Canada.

[11] S. Jadach, J.H. Kühn and Z. Wąs, (TAUOLA) Comp. Phys. Comm. **64** (1990) 275;
S. Jadach, *et al.*, (TAUOLA 2.4) Comp. Phys. Comm. **76** (1993) 361;
S. Jadach, B.F.L Ward and Z. Wąs, (KORALZ 3.8) Comp. Phys. Comm. **66** (1991) 276;

S. Jadach, B.F.L Ward and Z. Wąs, (KORALZ 4.0) Comp. Phys. Comm. **79** (1994) 503;
S. Jadach, B. F. Ward and Z. Was, (KORALZ 4.02) Comp. Phys. Comm. **124** (2000) 233.
Events were generated with KORALZ 4.02 setting $s'/s > 0.00156$ and TAUOLA 2.6 with four pion decays modelled according to:
R. Decker, M. Finkemeier, P. Heiliger and H. H. Jonsson, Z. Phys. **C70** (1996) 247.

[12] S. Jadach, W. Placzek and B.F.L. Ward, (BHWIDE) Phys.Lett. **B390** (1997) 298.

[13] T. Sjöstrand, Comp. Phys. Comm. **39** (1986) 347;
M. Bengtsson and T. Sjöstrand, Comp. Phys. Comm. **43** (1987) 367;
M. Bengtsson and T. Sjöstrand, Nucl. Phys. **B289** (1987) 810.

[14] OPAL Collab., P. Acton *et al.*, Z. Phys. **C58** (1993) 387.

[15] R. Battacharya, J. Smith and G. Grammer, Phys. Rev. **D15** (1977) 3267;
J. Smith, J.A.M. Vermaseren and G. Grammer, Phys. Rev. **D15** (1977) 3280.

[16] (PHOJET 1.05c used with JETSET 7.408):
R. Engel and J. Ranft, Phys. Rev. **D54** (1996) 4244;
R. Engel, Z. Phys. **C66** (1995) 203;
A. Buijs, W. G. Langeveld, M. H. Lehto and D. J. Miller, (TWOGEN) Comp. Phys. Comm. **79** (1994) 523.

[17] J. Hilgart, R. Kleiss, F. Le Diberder, Comp. Phys. Comm. **75** (1993) 191.

[18] J. Allison *et al.*, Nucl. Inst. and Meth. **A317** (1992) 47.

[19] R. Brun, F. Bruyant, M. Maire, A.C. McPherson, and P. Zanarini, *GEANT3*, CERN DD/EE/84-1 (1987).

[20] D. Karlen, Computers in Physics, 12:4 (1998) 380.

[21] M. Thomson, Nucl. Inst. and Meth. **A382** (1996) 553.

[22] ARGUS Collab., H. Albrecht *et al.*, Z. Phys. **C58** (1993) 61.

[23] J.H. Kühn and A. Santamaria Z. Phys. **C48** (1990) 445;
J.H. Kühn and E. Mirkes, Z. Phys. **C56** (1992) 661.

[24] N. Isgur, C. Morningstar and C. Reader, Phys. Rev. **D39** (1989) 1357.

[25] Y. Tsai, Phys. Rev. **D 13** (1976) 771.

[26] R. Barlow and C. Beeston, Comp. Phys. Comm. **77** (1993) 219.

[27] D. Bardin *et al.*, "ZFITTER: An Analytical program for fermion pair production in e+ e- annihilation", CERN-TH. 6443/92 (1992), hep-ph/9412201; D. Bardin, P. Christova, M. Jack, L. Kalinovskaya, A. Olchevski, S. Riemann and T. Riemann, Comput. Phys. Commun. **133** (2001) 229 [hep-ph/9908433].

[28] The Particle Data Group, D.E. Groom *et al.*, Eur. Phys. J. **C15** (2000) 1.
(URL: http://pdg.lbl.gov/).

[29] OPAL Collab., R. Akers *et al.*, Z. Phys. **C67** (1995) 45.

[30] P. R. Poffenberger, Z. Phys. **C71** (1996) 579.

[31] ALEPH Collab., D. Decamp *et al.*, Phys. Lett. **B265** (1991) 430;
ALEPH Collab., D. Buskulic *et al.*, Z. Phys. **C59** (1993) 369;
ALEPH Collab., D. Buskulic *et al.*, Z. Phys. **C69** (1996) 183.
Using all published ALEPH τ polarization measurements, ALEPH quotes combined results of $\mathcal{A}_\tau = 0.136 \pm 0.012 \pm 0.009$, $\mathcal{A}_\mathrm{e} = 0.129 \pm 0.016 \pm 0.005$, $\sin^2\theta^{\mathrm{lept}}_{\mathrm{eff}} = 0.2332 \pm 0.0014$.

[32] DELPHI Collab., P. Abreu *et al.*, Z. Phys. **C55** (1992) 555;
DELPHI Collab., P. Abreu *et al.*, Z. Phys. **C67** (1995) 183;
DELPHI Collab., P. Abreu *et al.*, Eur. Phys.J. **C14** (2000) 585-611.
Using all published DELPHI τ polarization measurements, DELPHI quotes combined results of $\mathcal{A}_\tau = 0.1359 \pm 0.0079 \pm 0.0055$, $\mathcal{A}_\mathrm{e} = 0.1382 \pm 0.0116 \pm 0.0005$, $\sin^2\theta^{\mathrm{lept}}_{\mathrm{eff}} = 0.23282 \pm 0.00092$.

[33] L3 Collab., O. Adriani *et al.*, Phys. Lett. **B294** (1992) 466.
L3 Collab., M. Acciarri *et al.*, Phys. Lett. **B341** (1994) 245;
L3 Collab., M. Acciarri *et al.*, Phys. Lett. **B429** (1998) 387.
Using all published L3 τ polarization measurements, L3 quotes combined results of $\mathcal{A}_\tau = 0.1476 \pm 0.0088 \pm 0.0062$, $\mathcal{A}_\mathrm{e} = 0.1678 \pm 0.0127 \pm 0.0030$, $\sin^2\theta^{\mathrm{lept}}_{\mathrm{eff}} = 0.2306 \pm 0.0011$.

[34] LEP Collaborations and the LEP Electroweak Working Group, *A Combination of Preliminary LEP Electroweak Results and Constraints on the Standard Model*, CERN-EP-2000-016, January 2000.
All the asymmetry measurements made at LEP, including some preliminary results and including the τ polarization, yields an average value of $\sin^2\theta^{\mathrm{lept}}_{\mathrm{eff}}$=0.23192±0.00023. The Standard Model fit to all LEP electroweak data, including M_W and the τ polarization, yields a value of $\sin^2\theta^{\mathrm{lept}}_{\mathrm{eff}}$=0.23150±0.00016.

The LEP average value from the forward-backward asymmetry from all leptons is $\sin^2\theta^{\mathrm{lept}}_{\mathrm{eff}}$=0.23107±0.00053; from the forward-backward hadronic charge asymmetry is $\sin^2\theta^{\mathrm{lept}}_{\mathrm{eff}}$=0.2321±0.0010; from the forward-backward asymmetry from c-quarks is $\sin^2\theta^{\mathrm{lept}}_{\mathrm{eff}}$=0.23255±0.00086; and from the forward-backward asymmetry from b-quarks is $\sin^2\theta^{\mathrm{lept}}_{\mathrm{eff}}$=0.23228±0.00036.

[35] SLD Collab., K. Abe *et al.*, Phys. Rev. Lett. **84** (2000) 5945.
This measurement of A_{LR} yields a value of $\sin^2\theta^{\mathrm{lept}}_{\mathrm{eff}}$=0.23097±0.00027.